Supplementary Information for

Synthesis and Characterization of Isostructural Annulated Actinocenes

Dominic R. Russo,[a,b] **, Jacob A. Branson,**[a,b] **, Sheridon N. Kelly,**[a,b] **, Asmita Sen,**[c] **, S, Olivia Gunther**[a] **, Appie Peterson,**[a] **, Patrick W. Smith,**[a] **, Erik T. Ouellette,**[a,b] **, John Arnold,**[a,b] **, Jochen Autschbach,**[c*] **, and Stefan G. Minasian**[a*]

[a]Chemical Sciences Division, Lawrence Berkeley National Laboratory, Berkeley, California, 94720, USA.
[b]Department of Chemistry, University of California, Berkeley, California, 94720, USA.
[c]Department of Chemistry, University of Buffalo; Buffalo, New York, 14260, USA.

*Corresponding authors: Jochen Autschbach and Stefan G. Minasian.
E-mail: jochena@buffalo.edu; sgminasian@lbl.gov

This PDF file includes:

> Supporting text
> Figs. S1 to S38
> Tables S1 to S25
> SI References

Table of Contents

Supplementary Information Text

1. General Considerations

Unless otherwise noted, all manipulations were carried out under an atmosphere of Ar or N_2 with exclusion of H_2O and O_2 using standard Schlenk technique or an inert atmosphere glovebox (MBraun) under Ar or N_2 for positive and negative pressure gloveboxes, respectively (Linde and AirGas). The negative pressure, inert-atmosphere transuranium glovebox was maintained under constant operational purge with a standalone Vacuum Atmosphere Genesis^{TM} O_2 and H_2O removal system. All glassware was dried in an oven at approximately 150 °C for at least 4 h or flame dried under vacuum prior to use. Celite (J.T. Baker) and molecular sieves (Aldrich) were dried under vacuum at a temperature of approximately 250 °C for 3 d in a quartz flask. n-Pentane, n-hexane, toluene (PhMe), 1,2-dimethoxyethane (DME), dichloromethane (CH_2Cl_2), and acetonitrile (MeCN) (Fisher Scientific or Avantor/VWR) were sparged with Ar for approximately 30 min, passed through a column of activated alumina (MBraun SPS-800), and stored over 3 Å molecular sieves. Tetrahydrofuran (THF) and diethyl ether (Et_2O) were vacuum transferred from a purple/red solution of Na/benzophenone then stored over 3 Å sieves. Pyridine (py) (Aldrich), fluorobenzene (PhF), and chlorobenzene (PhCl) (Avantor/VWR) were freeze-pump-thawed three times, stirred over CaH_2 for 3 d, distilled, and then stored over 3 Å sieves. Benzene-d_6 (C_6D_6) and toluene-d_8 (Cambridge Isotope Laboratories) were stored over 3 Å molecular sieves for 2 d and then vacuum-transferred from a purple Na/benzophenone solution prior to use. Pyridine-d_5 (C_6D_5N) and acetonitrile-d_3 (Cambridge Isotope Laboratories) were freeze-pump-thawed three times, stirred over CaH_2 for 3 d, distilled, and then stored over 3 Å molecular sieves. Allyl bromide (Aldrich) was washed with a saturated solution of $NaHCO_3$, dried over $MgSO_4$, distilled under Ar, freeze-pump-thawed three times, and stored over 3 Å molecular sieves. 1,6-Heptadiyne (Matrix Chemical) was fractionally distilled under partial vacuum (41 °C to 43 °C at approximately 60 torr) prior to use. Chlorotrimethylsilane (($CH_3)_3SiCl$) (TCI Ameirca) was fractionally distilled from CaH_2 twice. Iodotrimethylsilane (($CH_3)_3SiI$) (Alfa Aesar) was fractionally distilled from Cu powder and then stored over Cu beads in an Al-foil wrapped flask. Nujol mineral oil (Thermo Scientific) was sparged with Ar for approximately 20 min and then stirred over CaH_2 for 2 d, and finally filtered through a Celite pad. 18-crown-6 was recrystallized from MeCN then melted under vacuum until constant pressure to remove coordinated MeCN. Zn powder was cleaned according to literature.[1] $ThCl_4(DME)_2$, $ThI_4(DME)_2$, UCl_4, $UI_4(1,4-dioxane)_2$, and $UI_3(1,4-dioxane)_{1.5}$, $NpCl_4(DME)_2$, and $PuCl_4(DME)_2$ were prepared according to literature procedures with slight modification based on additional literature for the latter two precursors.[2–7] The ^{237}Np and ^{242}Pu stock solutions were prepared and purified as described previously.[7] Optima grade 37% HCl and 70% HNO_3 (Fishcer Scientific), hexachloropropene (Aldrich), CaH_2 (Aldrich), K metal (Aldrich), 2.2.2-cryptand (TCI America), and silica gel (80 to 200 mesh, J.T. Baker) were used as received.

Radiological Safety. ^{232}Th and ^{238}U are low activity α emitters, and were handled in monitored fume hoods or in an inert glovebox within a radiation laboratory equipped with α- and β-counting equipment. All transuranium studies were conducted within LBNL's heavy element radiological laboratory (HERL) with the entrance/exit monitored with a Canberra Sirius 5PAB personal contamination monitoring station. All work within HERL is conducted in fumehoods or in negative pressure gloveboxes equipped high efficiency particulate air (HEPA) filters. The ^{237}Np isotope ($t_{1/2}$ = 2.144 × 10^6 y; a = 0.7 mCi/g) undergoes α-decay to ^{233}Pa ($t_{1/2}$ = 26.975 d; a = 2.1 × 10^7 mCi/g), a high activity and high energy (570.3 keV) β emitter,[8–9] which decays into ^{233}U ($t_{1/2}$ = 1.5919 ×10^5 y; a = 9.7 × 10^{-3} Ci/g).[8] The ^{242}Pu isotope ($t_{1/2}$ = 3.73 × 10^{5}y; a = 3.9 mCi/g) undergoes α-decay to ^{238}U.[10] The ^{242}Pu stock solution used was 99.98 w/w% ^{242}Pu and is responsible for 84% of the α particles emitted. Additionally, a small amount of ^{240}Pu ($t_{1/2}$ = 6561 y; a = 1 mCi/g, < 0.02 w/w%) and ^{238}Pu ($t_{1/2}$ = 6561 y; a = 1 mCi/g, < 0.01 w/w%) were present.[11–12] A much smaller (<0.001% mass fraction) amount of ^{241}Pu ($t_{1/2}$ = 14.329 y; a = 1 mCi/g) does not contribute significantly to α particle emission, but results in a measurable amount of ^{241}Am ($t_{1/2}$ = 432.6 y; a = 3400 mCi/g)[13], which was separated before subsequent syntheses (*vide supra*)[7]. Due to their radiological hazards, quantitative UV-Vis spectra, FT-IR spectra, and elemental analyses of complexes containing ^{237}Np and ^{242}Pu radioisotopes could not be collected. All materials that were brought into the transuranium gloveboxes was done so without vacuum. All air sensitive non-rad solutions and solvents were prepared in a

separate non-rad glovebox using plastic micropipetters and were capped with PTFE-lined 22-400 (20 mL) or 13-425 (4 mL) caps before transfer into the transuranium gloveboxes.

2. Characterization and Physical Measurements

Nuclear magnetic resonance spectroscopy. Nuclear magnetic resonance (NMR) spectra were obtained on a Avance NEO 300 MHz Ultrashield NMR spectrometer at 298 K, unless otherwise noted. ^{1}H and ^{13}C NMR chemical shifts are reported in δ, parts per million. ^{1}H NMR are referenced to the residual ^{1}H resonances of the deuterated solvent; ^{13}C NMR are referenced to the ^{13}C resonance of the deuterated solvent.[14] The bulk of the NMR spectroscopy reported in this manuscript were collected in pyridine-d_5. While there appear to be some sporadic examples of minor impurities tabulated in this solvent, we could not obtain an expansive and citeable source. Table S25 lists the chemical shift and peak integration for relevant impurities to this manuscript. These spectra were collected in a manner similar to what has been described previously.[14] The peak position is listed, followed by the peak multiplicity, integration value, and proton assignment, where applicable. The multiplicity and shape are indicated by one or more of the following abbreviations: s (singlet); d (doublet); t (triplet); q (quartet); dd (doublet of doublets); td (triplet of doublets); ddd(doublet of doublet of doublets); dtt (doublet of triplet of triplets); m (multiplet); br (broad).

Optical spectroscopy. Fourier-transform infrared (FT-IR) spectra were recorded on a Bruker Vertex v80 spectrometer from 400 to 4000 $\mathrm{cm^{-1}}$ as nujol mulls sandwiched between two KBr plates. The peaks are listed in wavenumbers ($\mathrm{cm^{-1}}$). Their intensity is listed with the following abbreviations: vw (very weak); w (weak); m (medium); s (strong); vs (very strong); sh (shoulder); br (broad). All UV-Vis-NIR spectra were collected on a Cary 6000i between 1350 nm and 200 nm. The ^{237}Np and ^{242}Pu spectra were collected using a screw cap micro fluorescence quartz cuvette (Starna, clear sides) with a 1 cm path while the non-transuranium spectra were collected with screw cap semi-micro quartz qartz cuvettes (Starna, blacked-out sides) with a 1 cm path. The non-transuranium-containing solutions were also prepared by serial dilution with a combination of volumetric flasks and volumetric pipettes. Spectral plots shown in Figures S18 to S21 are truncated to a range of 200 to 700 nm; no strong transitions were observed at wavelengths greater than 700 nm at the concentrations used.

Single crystal X-ray diffraction. For all non-transuranium samples, single crystal samples were coated in Paratone-N oil for transport to diffraction facilities. Crystals of Th(hdcCOT)$_2$ and U(hdcCOT)$_2$ were mounted on a MiTeGen 100 μm Dual-Thickness MicroLoop for measurement on a Rigaku XtaLAB Synergy, Dualflex, HyPix diffractometer. Samples of Th(hdcCOT)$_2$ were sensitive to cryogenic temperatures, and could only be collected at ≥ 150 K. Samples of U(hdcCOT)$_2$ appeared less sensitive and were collected at both 100 K as well as 293 K. For Np(hdcCOT)$_2$ and Pu(hdcCOT)$_2$, in an inert atmosphere transuranium glovebox, a crystal was selected using a small digital microscope, swabbed in Paratone-N oil, secured to a MiTeGen loop with superglue for primary containment and encased in a MiTeGen polyester capillary for secondary containment. For Np(hdcCOT)$_2$, data was collected only at room temperature while for For Pu(hdcCOT)$_2$ data was collected both at room temperature and at 100 K. Single crystal X-ray diffraction measurements for hdcCOT and Pu(hdcCOT)$_2$ were performed at the Advanced Light Source (ALS) of LBNL Beamline 12.2.1, using a silicon double crystal monochromator to provide a beam of 17 keV (λ = 0.7288 Å) and the datasets collected at 100 K. For data collected at the ALS, data were collected on a Bruker D8 with PHOTON 100 detector. For data collected on the Rigaku diffractometer, CrysAlisPro (Rigaku, V1.171.40.47a, 2019) was used for the data collections and data processing, including a multi-scan absorption correction applied using the SCALE3 ABSPACK scaling algorithm within CrysAlisPro. For data collected on the Bruker diffractometer, the APEX3 software package and its associated programs (e.g. SAINT, SADABS) were used for the data collection, unit cell determination and refinement, integration, and absorption correction procedures.[15] For transuranium samples, at the time of publication, PLATON2 did not have scattering factors for elements beyond uranium when non-standard wavelengths are used, and therefore could not validate internally calculated f' and f" values. Unless otherwise noted below, the structures were solved with the ShelXT structure solution program using the Intrinsic Phasing solution method and by using Olex2

as the graphical interface. [16–17] The model was refined against F2 with version 2014/7 of SHELXL by full matrix least squares minimization. [18] Thermal parameters for all non-hydrogen atoms were refined anisotropically. Crystallographic renditions were generated using CrystalMaker®. [19]

Combustion analysis. Elemental analyses were determined at the Microanalytical Laboratory of the College of Chemistry, University.

3. Methods

Preparation of NiI$_2$(DME)$_2$. A modified procedure was used to prepare NiI$_2$(DME)$_2$. [20–21] Nickel powder (30.1 g, 513 mmol) was slurried in water (500 mL). The mixture was heated to 50 °C and I$_2$ (130 g, 512 mmol) was added in portions over 20 min. The mixture developed an intense green color. Once nearly all of the Ni metal powder was no longer clearly visible, the hot solution was filtered. The solution was then evaporated (approximately 60 °C) with a flow of air. Eventually, the dark green solution (and the incipient crystals formed during evaporation) turned into a purple-black crust which on standing turned back into a green slush. This material was collected and dried with triethylorthoformate according to a literature procedure. The material was then Soxhlet extracted using DME. Each extraction was carried out in 10 g batches with approximately 150 mL of DME in a Schlenk flask. A small amount of Celite was added to pad the frit of the thimble and help prevent clogging. The time for complete extraction was approximately 3 d (for each batch). Afterwards, the solid was collected by filtration to yield large red-orange crystals, which were briefly exposed to vacuum (approximately 5 min per batch) then stored in the freezer (total mass collected after all subsequent extractions 183 g, 87%). Lewis-base adducts of NiI$_2$ have previously been shown to have variable formula weight and are sensitive with respect to loss of DME. [21] The aforementioned method was found to consistently produce material most consistent with NiI$_2$(DME)$_2$. Elemental analysis found (calculated): C, 19.74 (19.50). H, 4.13 (4.09).


Synthesis of hdcCOT.
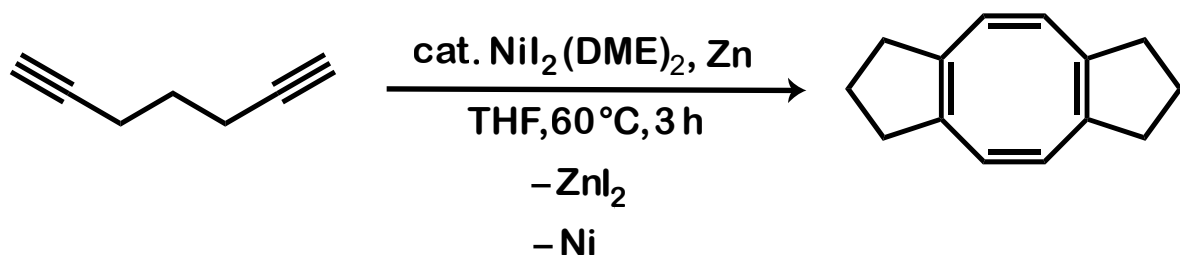
The neutral hdcCOT was synthesized by a modified literature procedure. [22–23] In a 250 mL Schlenk tube, 1,6-heptadiyne (g, mmol) along with approximately 100 mL of THF were added. In a separate 200 mL pear-shaped Schlenk flask, NiI$_2$(DME)$_2$ and Zn were added as solids. Both flasks were then chilled with an ice bath and then the THF solution of 1,6-heptadiyne was transferred onto the NiI$_2$(DME)$_2$/Zn mixture. The color quickly changed from orange-red to dark brown-black and a modest exotherm is observed. A reflux condenser was then attached to the flask, the ice bath was removed, and the reaction was set to reflux for 3 h. Over the course of the reflux, the reaction had turned from brown to jet black. Afterwards, the reaction mixture was left to room temperature and then volatiles were removed *in vacuo*. The black solids were extracted with nxn mL of *n*-hexane by centrifugation. The resulting yellow-orange supernatants were then combined and volatiles were removed *in vacuo*. *Note:* If the *n*-hexane supernatants are left to stand, over time an insoluble white solid begins to precipitate. The spectroscopic data were identical to what has been reported previously, but the ^{1}H and [13]C
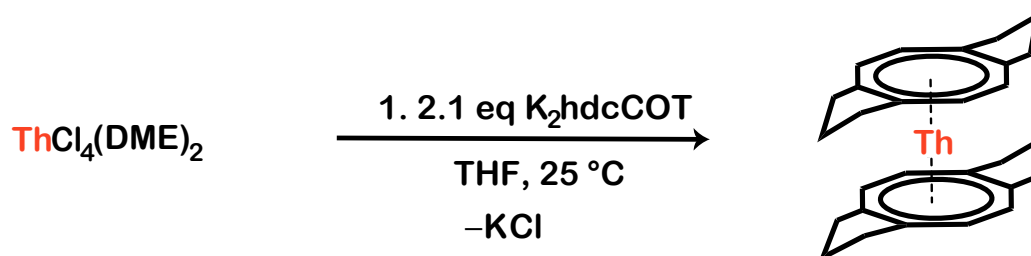
data are reported here in pyridine-d$_5$ for consistency, since it is the most common minor impurity. ^{1}H (py-d$_5$, 300 MHz): δ_H 5.69 (s, 4H, -CH=C), 2.19 (t, 8H, J = 7.5 Hz, C−$\underline{CH_2}$−CH$_2$) 1.68 (p, 4H, J = 7.8 Hz, C−CH$_2$−$\underline{CH_2}$) ppm. ^{13}C (75 MHz, py-d$_5$): δ_C = 140.54 (CH=$\underline{C}$), 130.50 ($\underline{CH}$=C), 37.61 (C−$\underline{CH_2}$−CH$_2$), 22.46 (C−CH$_2$−$\underline{CH_2}$) ppm. Elemental analysis, found (calculated): C, 90.96 (91.25); 8.70 (8.75).

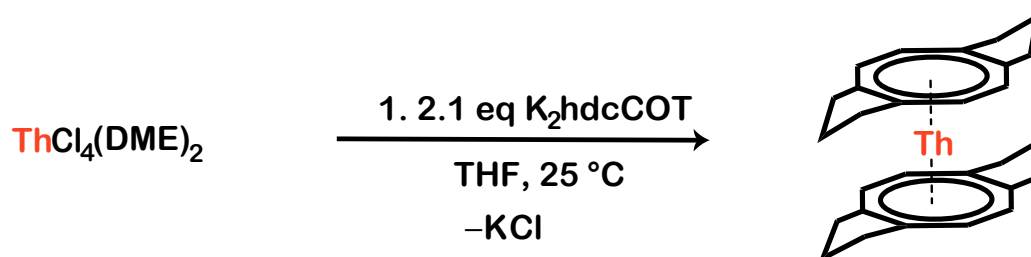
Synthesis of K$_2$hdcCOT.
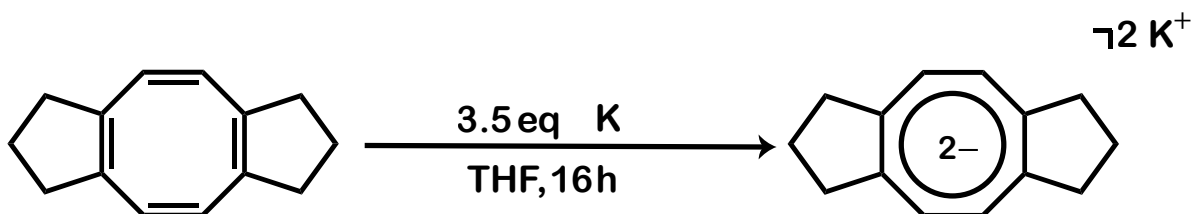
K$_2$hdcCOT was prepared by a modified literature procedure.[24]? In a glovebox, freshly cut and cleaned pieces of K metal (5.94 g, 152 mmol) were added to a 500 mL pear-shaped Schlenk flask along with a large PTFE stir bar. In a separate 200 mL pear-shaped Schlenk flask, recrystallized hdcCOT (7.998 g, 43.40 mmol) was dissolved in approximately 150 mL of THF. The flask containing the K was heated under vacuum with a butane Crème brûlée torch to make a K mirror. While cooling, the flask was rolled back-and-forth to coat the side walls with the rest of the K metal. Once all the K metal had crystallized, the flask was cool, and the stirring bar mobile, the THF solution of hdcCOT was transferred onto K. Immediately on contact, the golden-yellow solution changed to orange-brown and then later dark red. The solution was stirred for 24 h. The reaction mixture was then filtered with a Celite-padded Schlenk frit into a 500 mL pear-shaped Schlenk flask, yielding a clear, deep red solution. The excess K metal and small residual yellow solid were washed twice with 100 mL of fresh THF. The solution was concentrated *in vacuo* to approximately 100 mL then allowed to cool overnight at −20 °C, yielding yellow, plate-like crystals. The mother liquor was decanted at −20 °C; the flask of crystals was subsequently evacuated briefly then transferred into the glovebox. (Contemporaneously, volatiles from the mother liquor of this first crystallization were removed *in vacuo* and the ensuing solids were recombined with subsequent recrystallizations, see below). In the glovebox, the crystals were redissolved in a minimum amount of THF (approximately 60 mL) and transferred into a two 60 mL vials. The solutions were then allowed to cool at −35 °C for 24 h. Afterwards, the mother liquor was decanted from the recrystallized K$_2$hdcCOT and volatiles were removed *in vacuo*. The solids were triturated once with Et$_2$O followed by *n*-pentane twice yielding K$_2$hdcCOT as a donor-free, off-white solid (5.487 g, 20.90 mmol, 48% yield). In the glovebox, the mother liquor from the recrystallizaton was then recombined with the residual solids that did not initially crystallize for a second crop of crystals (3.931 g, 14.98 mmol). ^{1}H (300 MHz, py-d$_5$): δ_H = 6.58 (s, 4H, $\underline{CH}$=C), 4.02 (t, 8H, J = 6.6 Hz, C−$\underline{CH_2}$−CH$_2$), 2.15 (p, 4H, J = 7.4 Hz, C−CH$_2$−$\underline{CH_2}$) ppm. ^{13}C (75 MHz, py-d$_5$): δ_C = 99.72 (CH=$\underline{C}$), 87.75 ($\underline{CH}$=C), 45.91 (C−$\underline{CH_2}$−CH$_2$), 26.61 (C−CH$_2$−$\underline{CH_2}$). FT-IR (nujol mull) ν = 2973 (m) 2737 (m, sh), 2711 (w, sh) 2590 (vw), 2568 (vw), 2551 (vw), 1682 (w, br), 1287 (w), 1276 (w), 1262 (w, sh), 1218 (vw), 1192 (vw), 1132 (m), 1095 (m), 1038 (w), 980 (m), 933 (w), 864 (w), 847 (vw), 806 (w), 755 (s), 679 (w), 627 (m), 591 (w), 586 (w), 566 (vw) cm^{-1}. Elemental analysis, found (calculated): C, 63.91 (64.06); 6.19 (6.14).

Large scale synthesis of Th(hdcCOT)$_2$.

$$\text{ThCl}_4(\text{DME})_2 \quad \xrightarrow[\substack{\text{THF, 25 °C} \\ -\text{KCl}}]{\text{1. 2.1 eq K}_2\text{hdcCOT}} \quad \text{Th(hdcCOT)}_2$$

In a glovebox, ThCl$_4$(DME)$_2$ (4.047 g, 7.304 mmol) was added to a pear-shaped 200 mL Schlenk flask along with K$_2$hdcCOT (4.015 g, 15.30 mmol), and a PTFE coated magnetic stir bar. No reaction between the two solids was observed. The flask was transferred onto the line and approximately 100 mL of THF was transferred onto the mixture. The resulting mixture quickly turned from deep red to bright orange. The reaction is stirred for 16 h and then volatiles were removed *in vacuo*. The mixture was triturated twice with Et$_2$O and then twice with *n*-pentane. Afterwards, the mixture was extracted with 3×20 mL of PhCl and filtered over a Celite pad in a Schlenk frit into a 100 mL Schlenk tube. The filtrate solution was concentrated *in vacuo* (to approximately 20 mL) and then allowed to cool over night at −20 °C. The pale-yellow mother liquor was then decanted off the orange, plate-like crystals and residual volatiles were removed *in vacuo*. The dried crystals were then transferred into the glovebox, redissolved in a minimum amount of PhCl (*Note:* grinding of the crystals is necessary to improve the rate of dissolution) and allowed recrystallize at −35 °C overnight. The pale-yellow supernatant was then decanted and volatiles were removed *in vacuo* to yield Th(hdcCOT)$_2$ as red-orange crystals (3.394 g, 5.65 mmol, 77.6%). Crystals suitable for X-ray diffraction were grown from PhCl, but may also be grown from PhF (although over a longer time frame). ^{1}H NMR (300 MHz, py-d$_5$): δ_H = 6.52 (s, 8H, C$\underline{\text{H}}$=C), 3.84 (ddd, 8H, J = 13.7, 9.7, 7.4 Hz, C−C$\underline{\text{H}}_2$−CH$_2$), 3.55 (ddd, 8H, J = 13.7, 7.9, 3.3 Hz, C−C$\underline{\text{H}}_2$−CH$_2$), 2.23 (dtt, 4H, J = 11.8, 9.7, 7.9 Hz, C−CH$_2$−C$\underline{\text{H}}_2$), 2.04 (dtt, 4H, J = 10.9, 7.3, 3.3 Hz, C−CH$_2$−C$\underline{\text{H}}_2$) ppm. ^{13}C NMR (75 MHz, py-d$_5$): δ_C = 118.81 (CH=$\underline{\text{C}}$), 103.28 (C$\underline{\text{H}}$=C), 45.60 (C−$\underline{\text{C}}$H$_2$−CH$_2$), 25.70 (C−CH$_2$−$\underline{\text{C}}$H$_2$). FT-IR (nujol mull): ν = 3174 (w), 2030 (vw). 1958 (vw), 1786 (vw), 1767 (vw), 1648 (w), 1210 (vw), 1169 (m), 1153 (m), 1106 (vw), 1073 (vw), 1037 vw), 995 (vw), 967 (w), 937 (w), 918 (vw), 890 (w), 843 (w), 784 (w), 764 (m), 722 (s), 660 (vw), 639 (vw), 594 (vw), 551 (w), 443 (br) cm^{-1}. Elemental analysis, found (calculated): C, 55.73 (55.97); 5.63 (5.48).

Small scale synthesis of Th(hdcCOT)$_2$.

$$\text{ThCl}_4(\text{DME})_2 \quad \xrightarrow[\substack{\text{THF, 25 °C} \\ -\text{KCl}}]{\text{1. 2.1 eq K}_2\text{hdcCOT}} \quad \text{Th(hdcCOT)}_2$$

In a glovebox, ThCl$_4$(DME)$_2$ (2.41 mg, 4.35 µmol) was added to a 20 mL vial along with a glass coated magnetic stir bar and approximately 1 mL of THF. A solution of K$_2$hdcCOT (26.7 mg, 101.7 µmol) was prepared in a separate 20 mL vial with 10.0 mL of THF ([K$_2$hdcCOT] = 10.2 mM). and then 891 µL was added to the suspension

of $ThCl_4(DME)_2$. The mixture quickly changed from red to bright orange. The reaction was stirred for 16 h and then volatiles were removed *in vacuo*. The mixture was triturated twice with Et_2O and then twice with *n*-pentane. Afterwards, the mixture was extracted with 4×4 mL of PhCl by centrifugation in 10 mL glass, PTFE-caped centrifuge tubes at 4000 rpm for 20 min (i.e., two sets of 4 mL of PhCl were used to extract initially into two separate centrifuge tubes and then another two sets of 4 mL were used to extract a second time into the same centrifuge tubes). The supernatants were then filtered through a glass Pasteur pipette that was plugged with glass filter paper and a pad of Celite. The filtrate solution was concentrated *in vacuo* (to approximately 2 mL) and then allowed to cool over night at $-35\,°C$. The pale-yellow mother liquor was then decanted off the orange, plate-like crystals and residual volatiles were removed *in vacuo*. (2.33 mg, 4.35 μmol, 89%). Spectroscopic analysis of the product from this scale reaction were identical to those previously mentioned.
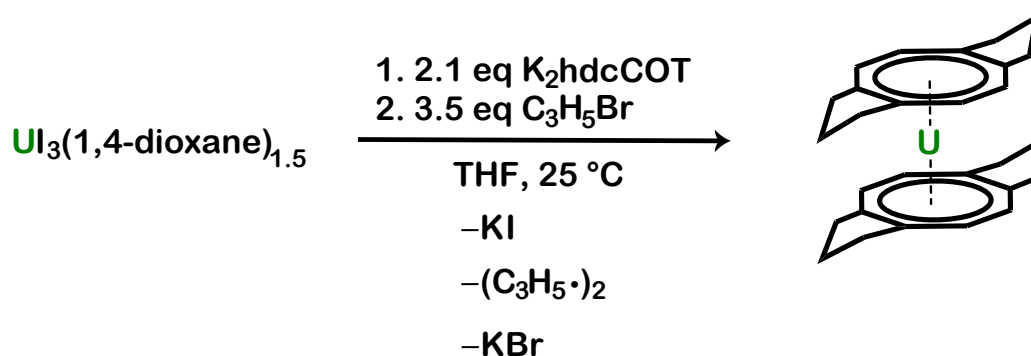

Synthesis of $U(hdcCOT)_2$ from $UI_3(1,4-dioxane)_{1.5}$.

Large scale synthesis of $U(hdcCOT)_2$ from $UI_3(1,4-dioxane)_{1.5}$.
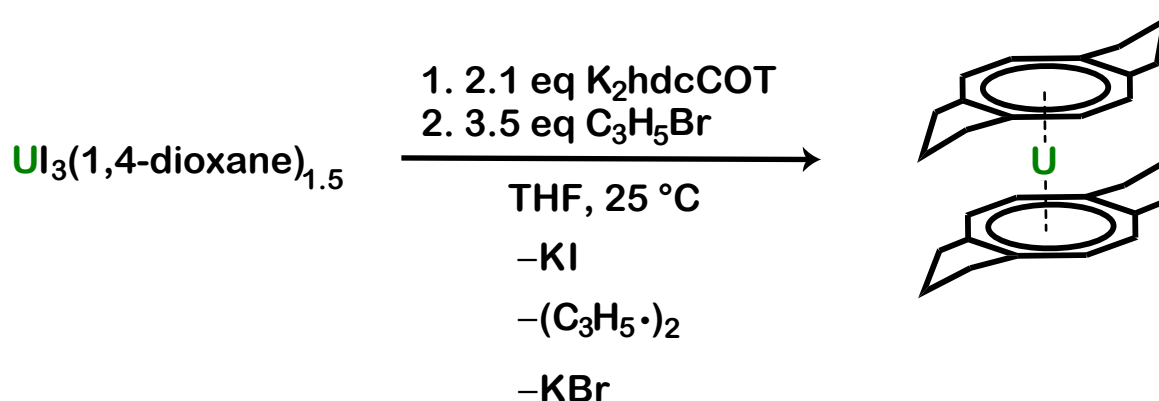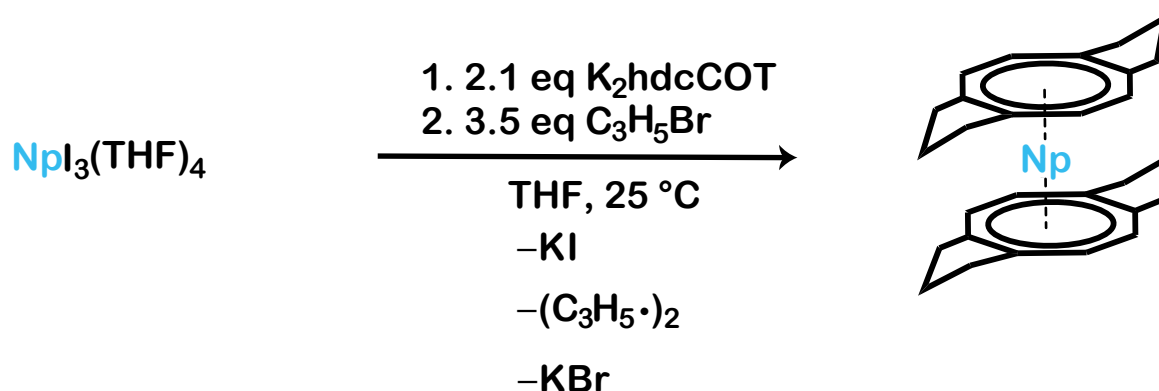

In a glovebox, $UI_3(1,4-dioxane)_{1.5}$ (10.549 g, 14.05 mmol) was added to a pear-shaped 500 mL Schlenk flask along with $K_2hdcCOT$ (7.743 g, 29.50 mmol), and a PTFE coated magnetic stir bar. No reaction between the two solids was observed. The flask was transferred onto the line and THF was transferred onto the mixture. The resulting mixture quickly turned from deep red to purple-brown. The reaction was stirred for 16 h. Afterwards, allyl bromide (4.5 mL, 6.0 g, 52.1 mmol) was added *via* syringe over the course of approximately 5 min. No exotherm was observed, but the solution quickly developed a dark olive green color. The reaction was allowed to stir for an additional 16 h. Volatiles were removed *in vacuo*. The mixture was triturated twice with Et_2O and then twice with *n*-pentane. Afterwards, the mixture was extracted with 4×50 mL of PhMe and filtered over a Celite pad in a Schlenk frit into a 250 mL Schlenk tube. The solution was concentrated *in vacuo* (approximately 50 mL) and then allowed to cool over night at $-20\,°C$. The green-brown mother liquor was then decanted off the crystals and residual volatiles were removed *in vacuo*. The crystals were then transferred into the glovebox, redissolved in a minimum quantity (approximately 40 mL or two scintillation vials) of PhMe (*Note:* grinding of the crystals is necessary to improve the rate of dissolution), and allowed to recrystallize at $-35\,°C$ overnight. The olive green supernatant was then decanted and residual volatiles were removed *in vacuo* to yield $U(hdcCOT)_2$ as extremely dark olive green-brown crystals (7.433 g, 12.25 mmol, 87.2%). ^{1}H NMR (300 MHz, py-d_5): $\delta_H =$ 27.17 (dt, 8H, $J = 16.4$, 8.4 Hz, C–$\underline{CH_2}$–CH_2), -8.41 (dt, 4H, $J = 14.2$, 7.6 Hz, C–CH_2–$\underline{CH_2}$), -18.55 (ddd, 8H, $J = 16.2$, 8.2, 3.1 Hz, C–$\underline{CH_2}$–CH_2), -34.71 (dt, 4H, $J = 22.6$, 8.5 Hz, C–CH_2–$\underline{CH_2}$), -39.43 (s, 8H, $\underline{CH}$=C) ppm. ^{13}C NMR (75 MHz, py-d_5): $\delta_C = 326.57$ (CH=$\underline{C}$), 294.58 ($\underline{CH}$=C), 11.47 (C–$\underline{CH_2}$–CH_2), -35.66 (C–$\underline{CH_2}$–CH_2) ppm. FT-IR (nujol mull): $\nu = 3184$ (vw), 1673 (vw), 1291 (s), 1276 (m), 1261 (s), 1235 (m), 1174(w), 1133 (s), 1115 (s), 1105 (s), 1079 (s), 1060 (m), 1041 (m), 991 (w), 953 (m), 935 (m), 892 (vw), 867 (vw), 833 (w), 821 (w), 797 (vw), 746 (m), 737 (s), 722 (m), 634 (vw), 628 (vw), 587 (vw), 567 (vw), 547 (vw), 525 (vw), 438 (br, m) cm^{-1}. Elemental analysis, found (calculated): C, 55.26 (55.40); 5.54 (5.30).

Small scale synthesis of U(hdcCOT)$_2$ from UI$_3$(1,4−dioxane)$_{1.5}$.

$$UI_3(1,4\text{-dioxane})_{1.5} \xrightarrow[\substack{\text{THF, 25 °C} \\ -KI \\ -(C_3H_5\cdot)_2 \\ -KBr}]{\substack{\text{1. 2.1 eq K}_2\text{hdcCOT} \\ \text{2. 3.5 eq C}_3\text{H}_5\text{Br}}}$$

In a glovebox, UI$_3$(1,4−dioxane)$_{1.5}$ (3.91 mg, 2.60 μmol) was added to a 20 mL vial along with a glass coated magnetic stir bar and approximately 1 mL of THF. A solution of K$_2$hdcCOT (14.8 mg, 56.4 μmol) was prepared in a separate 20 mL vial with 4.5 mL of THF ([K$_2$hdcCOT] = 12.5 mM). and then 871 μL (2.86 mg, 10.9 μmol) was added to the suspension of UI$_3$(1,4−dioxane)$_{1.5}$. The mixture quickly changed from purple to brown. The reaction was stirred for 16 h. In a separate 20 mL vial, a solution of allyl bromide (500 μL, 0.70 g, 6.0 mmol) was prepared in 10.000 mL of THF (using a volumetric flask, [C$_3$H$_5$Br] = 580 mM). A 35 μL aliquot of this allyl bromide solution was then added to the brown reaction mixture, which quickly turned dark olive green. The mixture was allowed to stir for 4 h and then volatiles were removed *in vacuo*. The resulting residue was triturated twice with Et$_2$O and then twice with *n*-pentane. Afterwards, the solid residues were extracted with 4×4 mL of PhMe by centrifugation in 10 mL glass, PTFE-caped centrifuge tubes at 4000 rpm for 20 min (i.e., two sets of 4 mL of PhMe were used to extract initially into two separate centrifuge tubes and then another two sets of 4 mL were used to extract a second time into the same centrifuge tubes). The supernatants were then filtered through a glass Pasteur pipette that was plugged with glass filter paper and a pad of Celite. The filtrate solution was concentrated *in vacuo* (to approximately 2 mL) and then allowed to cool over night at −35 °C. The pale-yellow mother liquor was then decanted off the orange, plate-like crystals and residual volatiles were removed *in vacuo*. (2.33 mg, 4.35 μmol, 89%). Spectroscopic analysis of the product from this scale reaction were identical to those previously mentioned.
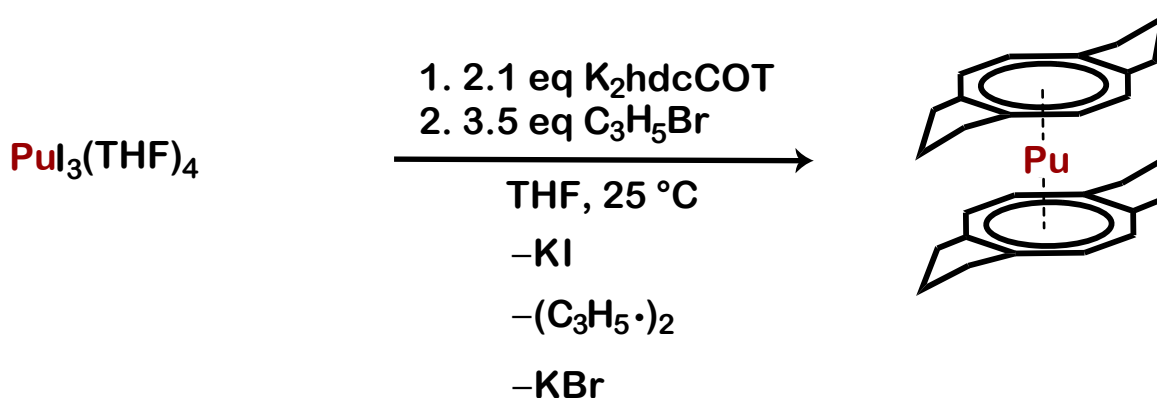

Synthesis of Np(hdcCOT)$_2$ from NpI$_3$(THF)$_4$.

$$NpI_3(THF)_4 \xrightarrow[\substack{\text{THF, 25 °C} \\ -KI \\ -(C_3H_5\cdot)_2 \\ -KBr}]{\substack{\text{1. 2.1 eq K}_2\text{hdcCOT} \\ \text{2. 3.5 eq C}_3\text{H}_5\text{Br}}}$$

NpI$_3$(THF)$_4$ was prepared by a modified literature procedure.[25] In a glovebox, an aliquot of a NpCl$_4$(DME)$_2$ solution (2.5 mg, 4.5 μmol, 1.1 mg Np^{4+} ions) in THF was transferred into a 4 mL vial along with a glass magnetic stir bar. The solution was brought to a residue, suspended in 500 μL of Et$_2$O, and then neat (pre-filtered) (CH$_3$)$_3$SiI (20 μL, 28 mg, 140 μmol) was added. After approximately 5 min, *n*-pentane (1000 μL) was added then the orange supernatant was decanted. The black precipitate was then washed with portions of Et$_2$O (2×1000 μL)

and n-pentane (2×1000 μL). Each time, the solids were allowed to settle in the freezer for 10 min and the supernatants were decanted and collected in a separate vial. The solids were then slurried in THF (500 μL), yielding putative $NpI_3(THF)_4$ as an orange solid. A 1000 μL aliquot of a $K_2hdcCOT$ solution in THF ($[K_2hdcCOT]$ = 9.33 mM → 9.33 μmol, 2.45 mg) was then added to the mixture of $NpI_3(THF)_4$ and stirred for 16 h. The resulting mixture quickly turned from red to brown. A 30 μL aliquot of an allyl bromide solution ($[C_3H_5Br]$ = 580 mM, → 17.4 μmol, 2.10 mg) was then added and stirred for 10 min. Volatiles were then removed by evaporation with the assistance of an aquarium pump and then the residues were triturated twice Et_2O (2×500 μL) followed by n-pentane (1×500 μL); each time being removed by evaporation with the assistance of an aquarium pump. The residue was then extracted with PhMe (2×500 μL) and centrifuged (in a 2 mL plastic centrifuge tube) for 5 min. The supernatant was then decanted into a new 4 mL vial and evaporated back down to a cherry red residue with the aquarium pump. This was re-dissolved in a minimum amount of 1:1 PhMe:n-hexane and allowed to cool at −35 °C overnight. The orange supernatant was then decanted off and the solids dried by evaporation, yielding $Np(hdcCOT)_2$ as a dark orange-brown crystalline solid (~2 mg, 3.30 μmol, ~70%). In a slightly larger scale follow-up synthesis, a similar procedure was used: $NpCl_4(DME)_2$ (3.6 mg, 6.5 μmol was again converted to $NpI_3(THF)_4$. A THF solution of $K_2hdcCOT$ (11 mM, 1.2 mL, 14 μmol, 3.6 mg) was then added and stirred overnight. The dark brown reaction mixture was then transferred to a centrifuge tube and the supernatant decanted into a new 4 mL vial. Afterwards, a THF solution of allyl bromide (11 mM, 2.0 mL, 23 μmol, 2.77 mg) was then added, and the reaction mixture was stirred for 1 h. The reaction mixture was centrifuged a second time and the supernatant was decanted into a 4 mL vial and evaporated to a residue with the assistance of an aquarium pump yielding $Np(hdcCOT)_2$ as an orange-brown solid, which was crystallized from a minimum amount of n-pentane at −35 °C (3.35 mg, 86%). *Note:* The NMR spectral assignments for $Np(hdcCOT)_2$ are very tentative with no observable ^{13}C resonances (even during heteronuclear 2D measurements), extremely broad ^1H resonances, and miscellaneous impurities such as solvent and neutral hdcCOT present. The current assignments provided herein are largely based on the spectral assignments for 1,1',3,3',5,5',7,7'-octamethylneptunocene.[26] ^1H NMR (300 MHz, py-d_5): δ_H = 37.71 (br s, 8H, C−$\underline{CH_2}$−CH_2), 1.23 (br s, 4H, C−CH_2−$\underline{CH_2}$), −5.12 (br s, 8H, C−$\underline{CH_2}$−CH_2), −18.82 (br s, 4H. C−CH_2−$\underline{CH_2}$), −36.21 (br s, 8H, $\underline{CH}$=C) ppm.

Synthesis of Pu(hdcCOT)$_2$ from PuI$_3$(THF)$_4$.

PuI$_3$(THF)$_4$

1. 2.1 eq K$_2$hdcCOT
2. 3.5 eq C$_3$H$_5$Br

THF, 25 °C

−KI

−(C$_3$H$_5$·)$_2$

−KBr

Pu

PuI$_3$(THF)$_4$ was prepared by a modified literature procedure.[25] In a glovebox, an aliquot of a $PuCl_4(DME)_2$ solution (2.5 mg, 4.5 μmol, 1.1 mg of Pu^{4+} ions) in DME was transferred into a 4 mL vial along with a glass magnetic stir bar. The solution was brought to a residue by evaporation with the assistance of an aquarium pump, suspended in 500 μL of Et_2O, and then neat (pre-filtered) $(CH_3)_3SiI$ (20 μL, 28 mg, 140 μmol) was added. After approximately 5 min, n-pentane (1000 μL) was added. The mixture was left to cool in the freezer for 10 min and then the supernatant was decanted into a separate vial. The slightly pale-green precipitate was then washed with Et_2O (2×1000 μL) and n-pentane (2×1000 μL). Each time, the solids were allowed to settle in the freezer for 10 min and the supernatants were decanted and collected in a separate vial. The solids were then slurried in

THF (500 μL), yielding putative $PuI_3(THF)_4$ as an off-white solid. A 1000 μL aliquot of a K_2hdcCOT solution in THF ($[K_2$hdcCOT] = 9.33 mM → 9.33 μmol, 2.45 mg) was then added to the mixture of $PuI_3(THF)_4$. The reaction mixture was then allowed to stir for 16 h, although the mixture had turned from red to lime green within several minutes of stirring. A 30 μL aliquot of a allyl bromide solution ($[C_3H_5Br]$ = 520 mM, → 15.6 μmol, 1.89 mg) was then added and stirred for 10 min. Immediately on addition, the solution turned from green to dark red, Volatiles were then removed by evaporation with the assistance of an aquarium pump and then the residues were triturated with Et_2O (2×500 μL) followed by *n*-pentane (1×500 μL); each time, volatiles were removed by evaporation with the assistance of an aquarium pump. The residue was then extracted with PhMe (2×500 μL portions of) and centrifuged (in a 2 mL plastic centrifuge tube) for 5 min. The supernatant was then decanted (presumably away from KI and KBr from the transmetallation and oxidation, respectively), transferred to a 4 mL vial, and then evaporated to a cherry red residue with the assistance of an aquarium pump. This was re-dissolved in a minimum amount of *n*-hexane and allowed to cool at −35 °C overnight. The pale red supernatant was then decanted off and the solids dried by evaporation, yielding $Pu(hdcCOT)_2$ as a dark red crystallinfe solid (~2 mg, 3.28 μmol, ~70%). ^{1}H NMR (300 MHz, py-d_5): δ_H = 9.96 (s, 8H, C̲H̲=C), 4.16 (dt, 4H, *J* = 13.7, 8.1, 2.7 Hz, C–CH$_2$–C̲H̲$_2$), 3.89 (ddd, 8H, *J* = 16.2, 8.2, 3.1 Hz, C–C̲H̲$_2$–CH$_2$, 2.44 (dt, 4H, *J* = 11.2, 7.7 Hz, C–CH$_2$–C̲H̲$_2$), 1.25 (ddd, 8H, *J* = 13.7, 10.2, 7.7 Hz, C–C̲H̲$_2$–CH$_2$) ppm. ^{13}C NMR (75 MHz, py-d_5): δ_C = 104.66 (CH=C̲), 88.58 (C̲H̲=C), 53.33 (sp^2-C–C̲H̲$_2$–CH$_2$), 26.55 (sp^2-C–CH$_2$–C̲H̲$_2$) ppm.

4. Spectroscopy

NMR spectra.
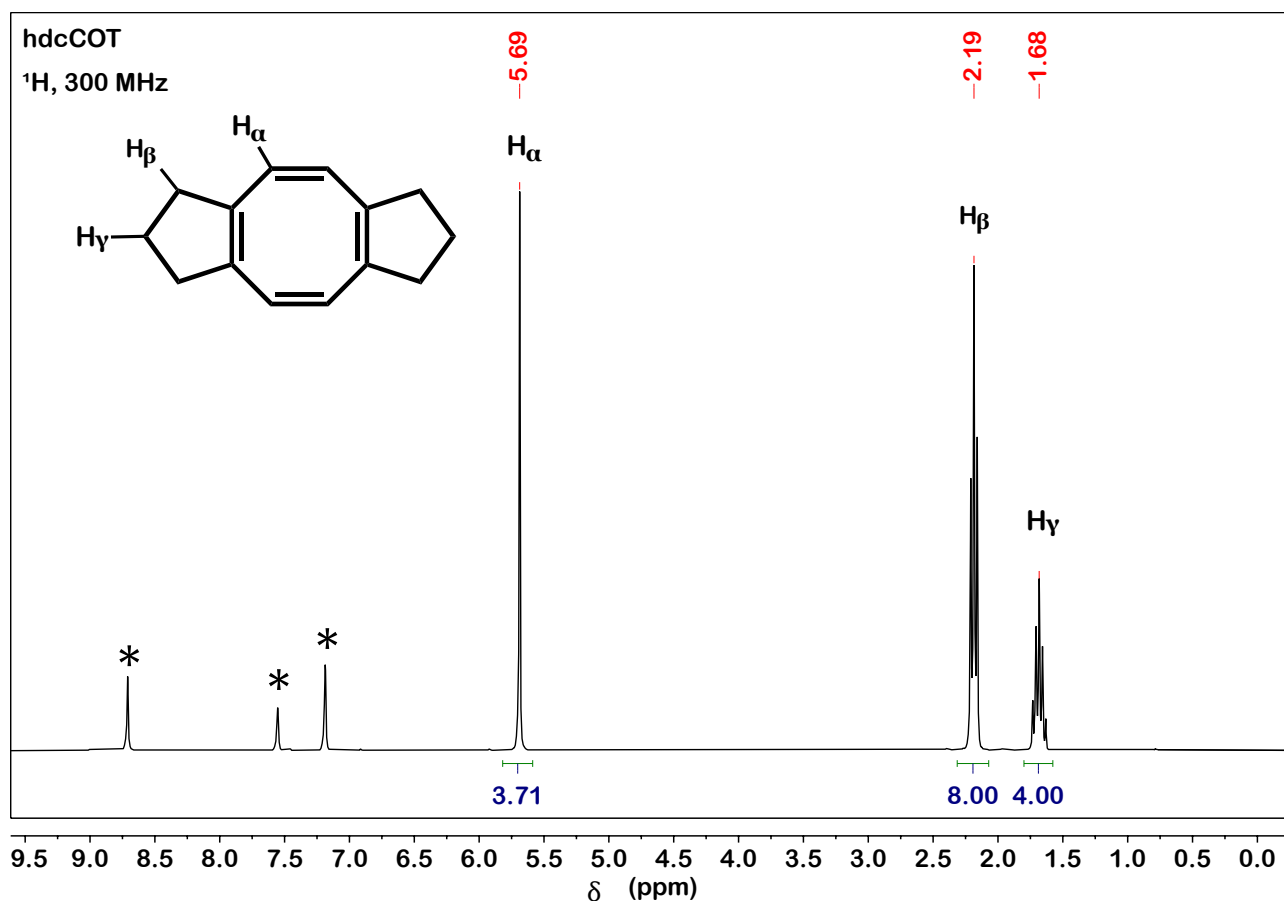
Fig. S1. ^{1}H NMR spectrum for hdcCOT. Peaks from residual C_5D_4HN are marked with an asterisk.
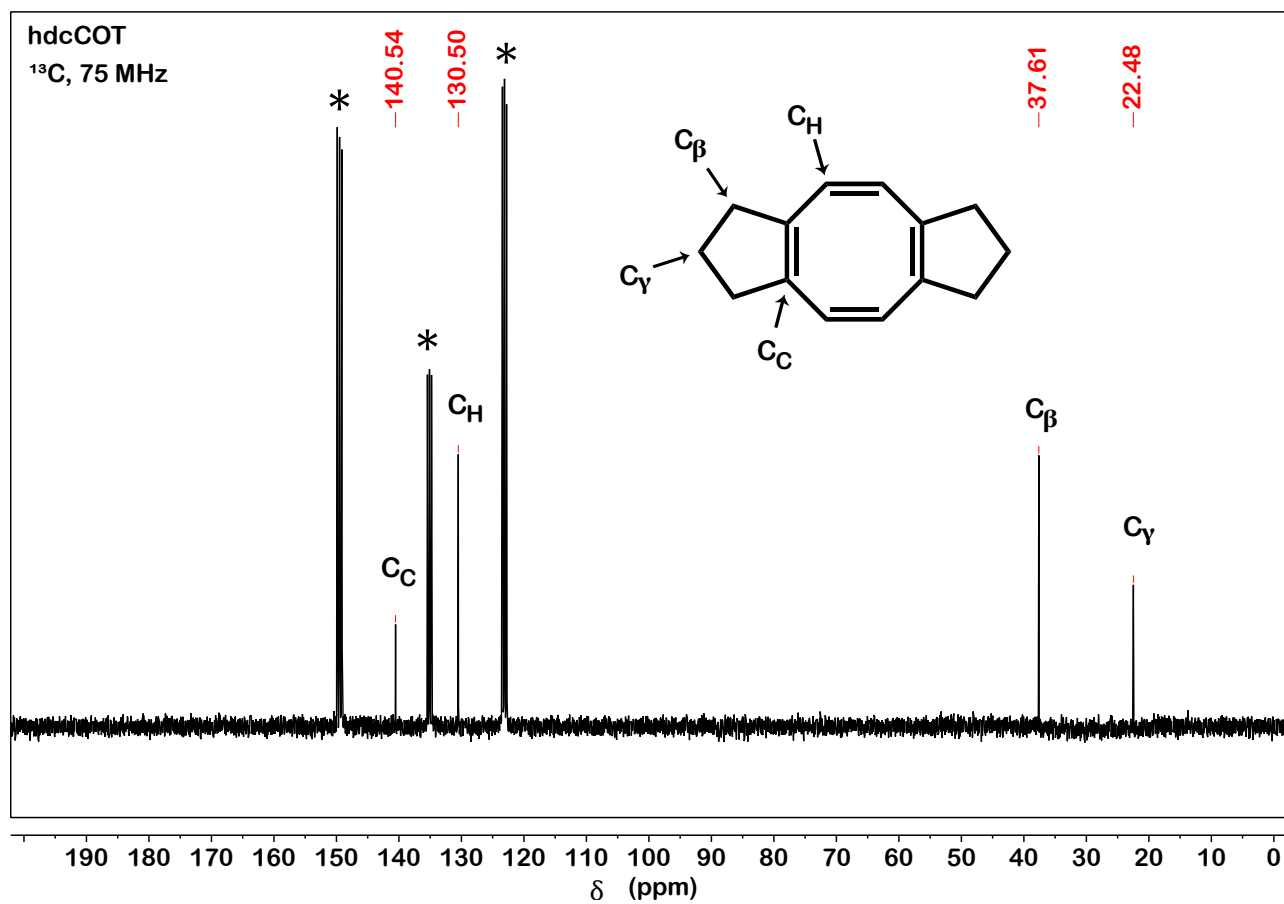
Fig. S2. $^{13}C\{^1H\}$ NMR spectrum for hdcCOT. Peaks from residual C_5D_4HN are marked with an asterisk.

Fig. S3. ^{1}H NMR spectrum for K_2hdcCOT. Peaks from residual C_5D_4HN are marked with an asterisk.

Fig. S4. $^{13}C\{^{1}H\}$ NMR spectrum for $K_2hdcCOT$. Peaks from residual C_5D_4HN are marked with an asterisk.
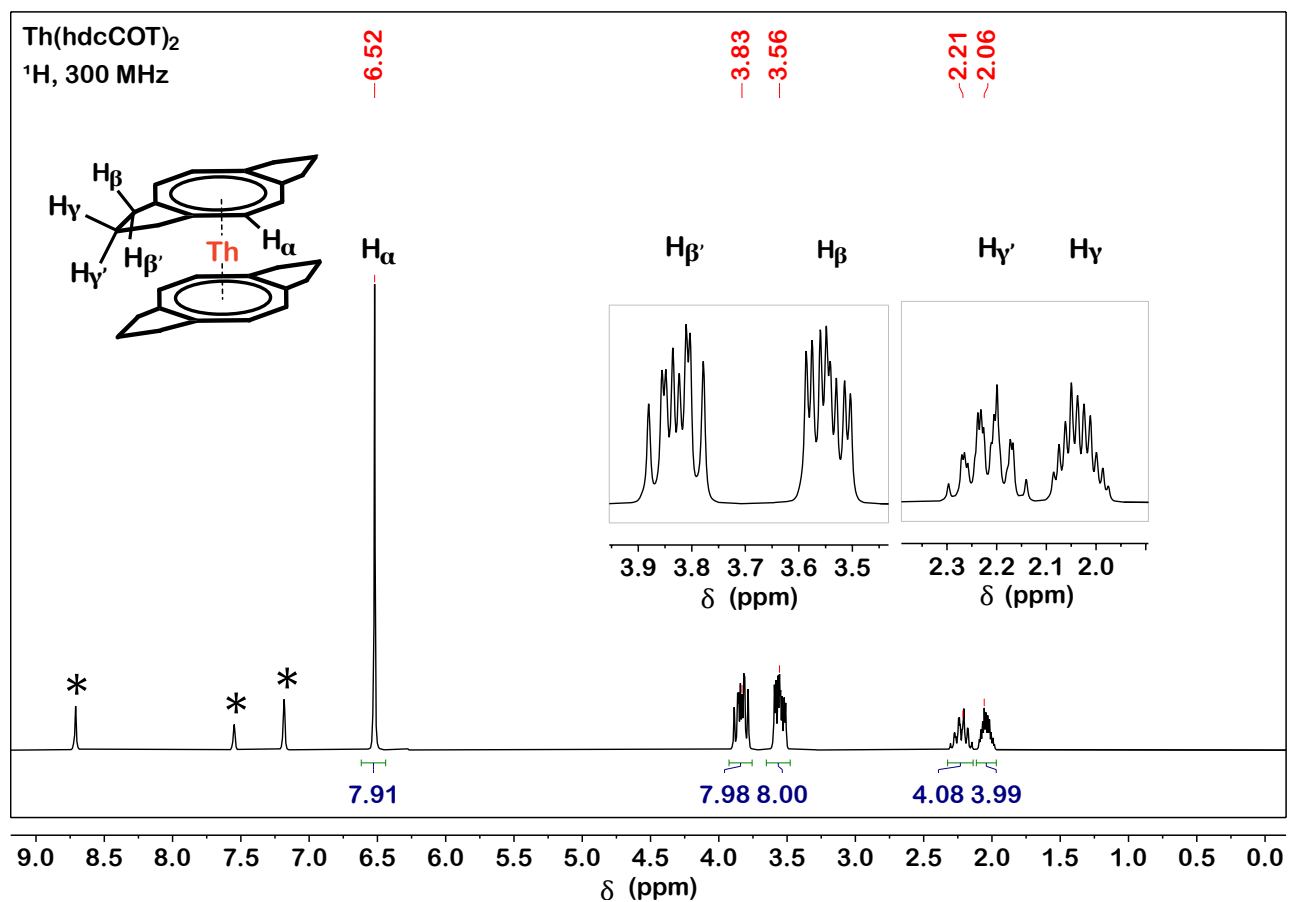
Fig. S5. ^{1}H NMR spectrum for Th(hdcCOT)$_2$. Peaks from residual C$_5$D$_4$HN are marked with an asterisk.
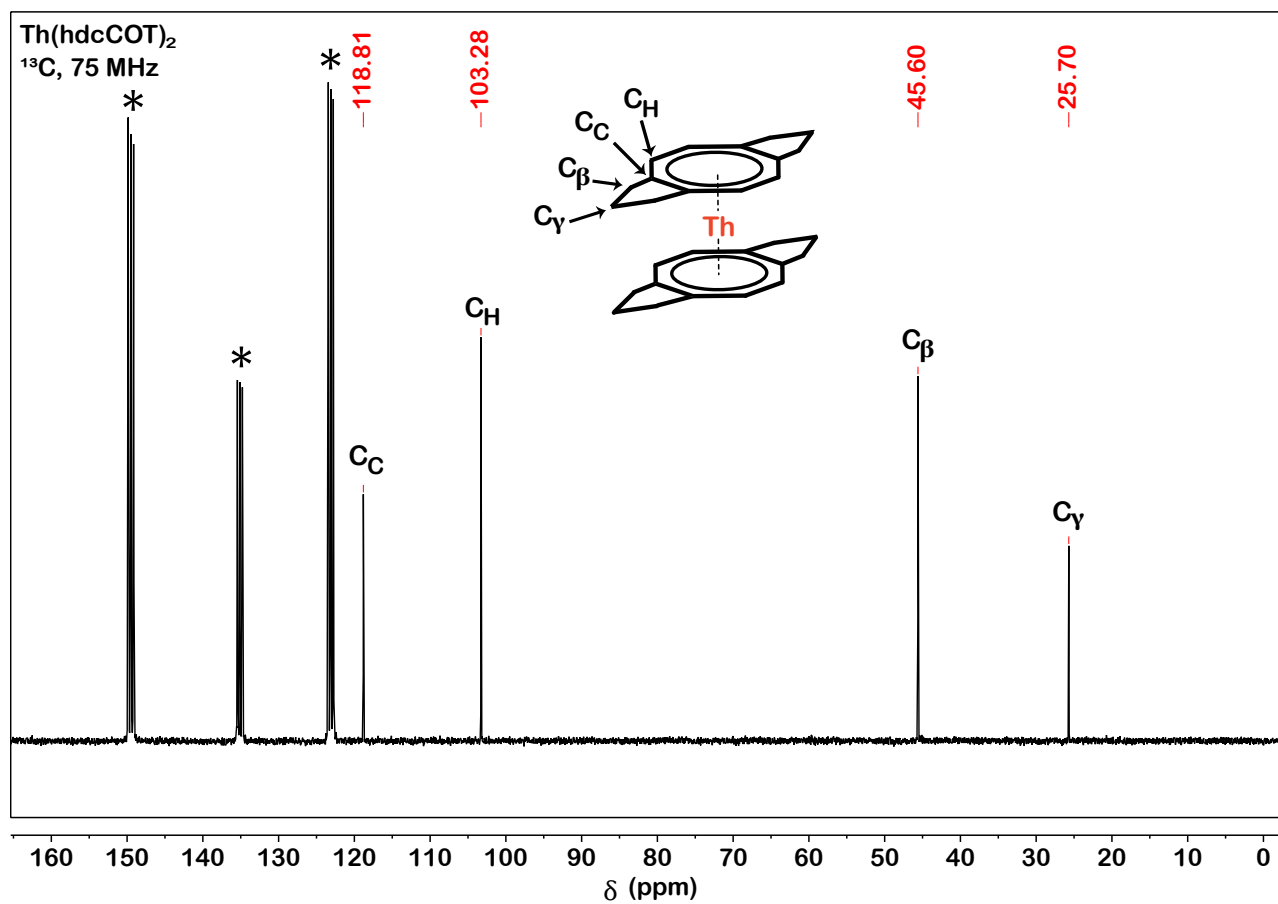
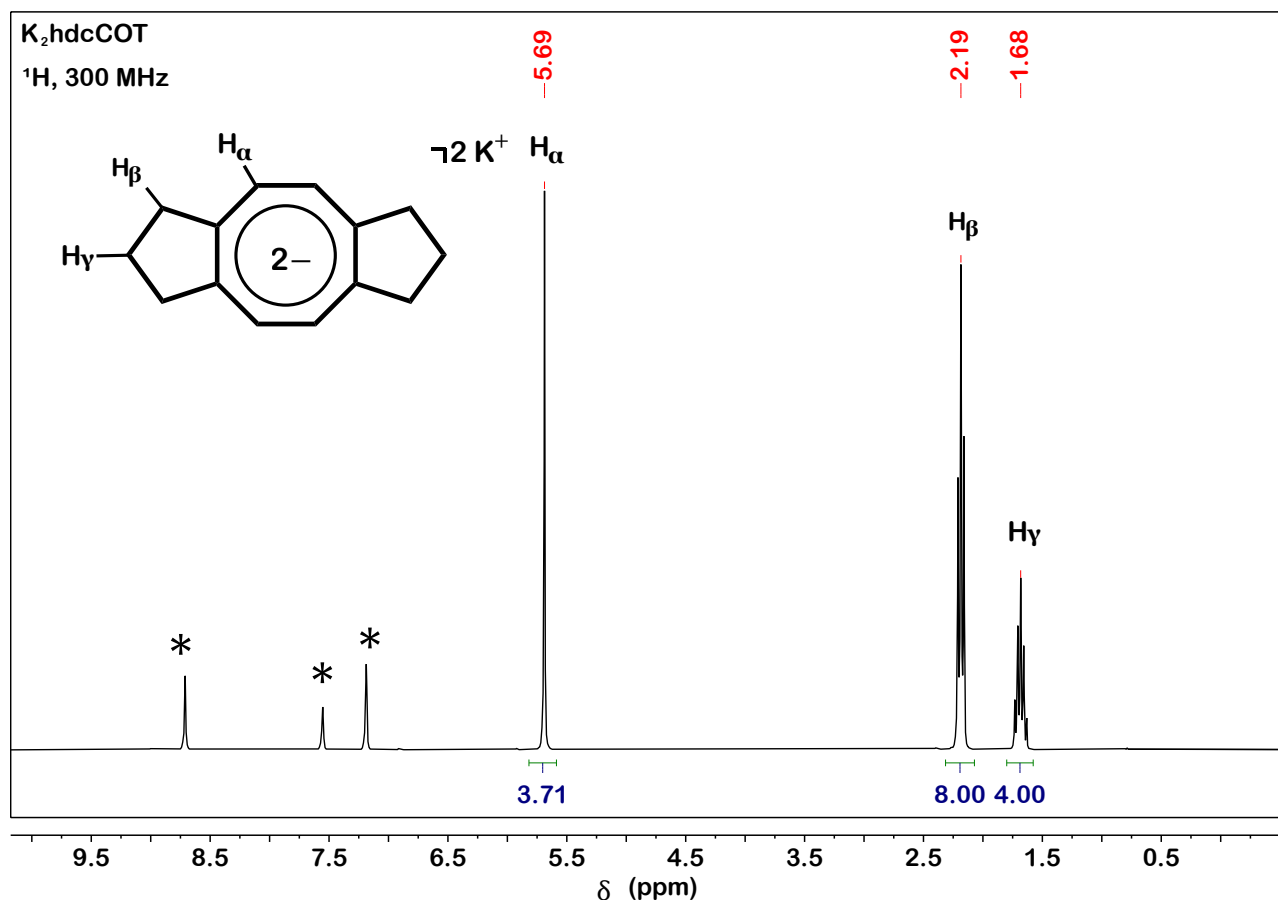**Fig. S6.** $^{13}C\{^1H\}$ NMR spectrum for Th(hdcCOT)$_2$. Peaks from residual C_5D_4HN are marked with an asterisk.

Fig. S7. $^{13}C\{^1H\}$-^1H HSQC 2D NMR spectrum for Th(hdcCOT)$_2$. The ^{13}C resonance with no cross peak is assigned as the completely substituted sp^2 carbon within the [8]annulene ring. Cross peaks from residual C$_5$D$_4$HN are marked with an asterisk.
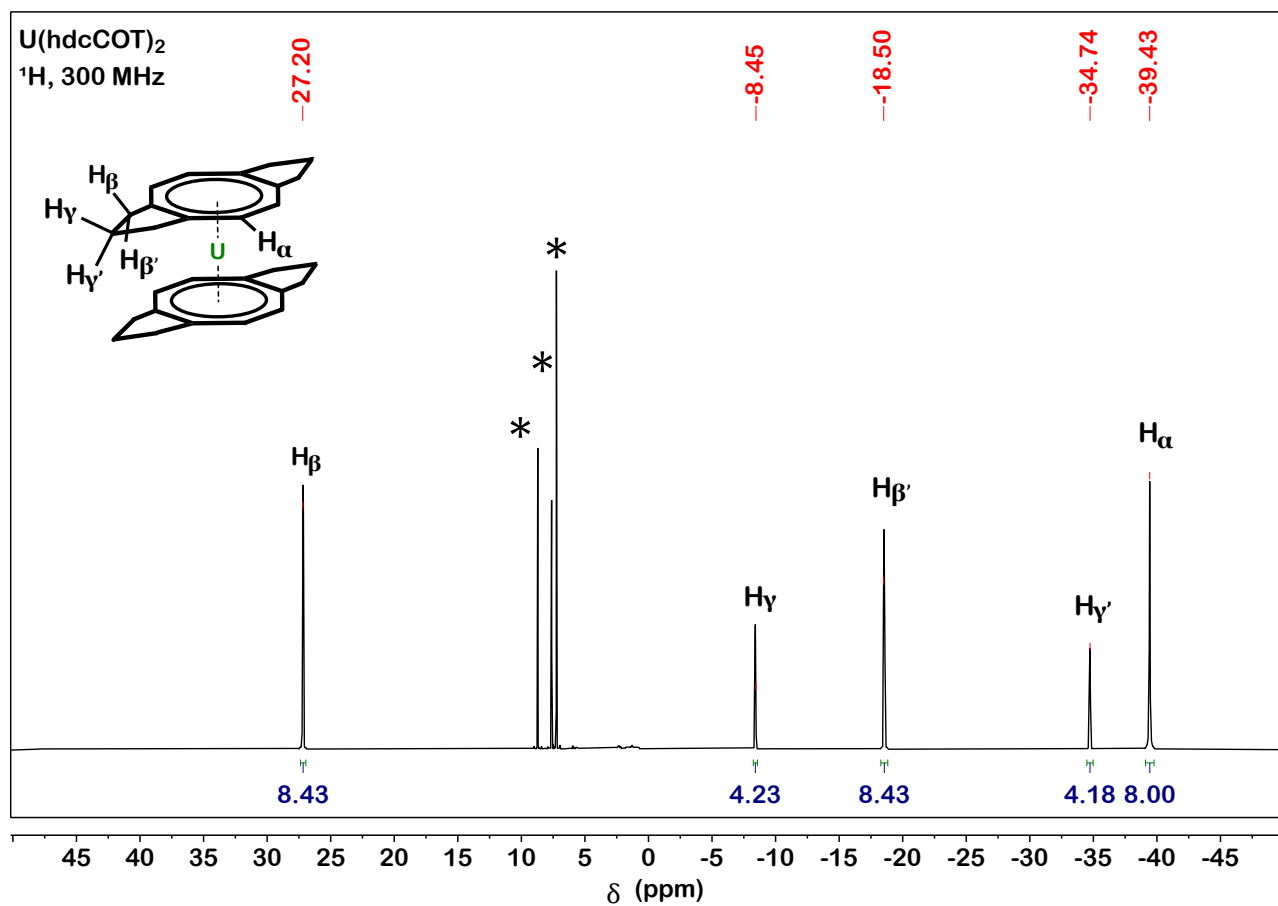
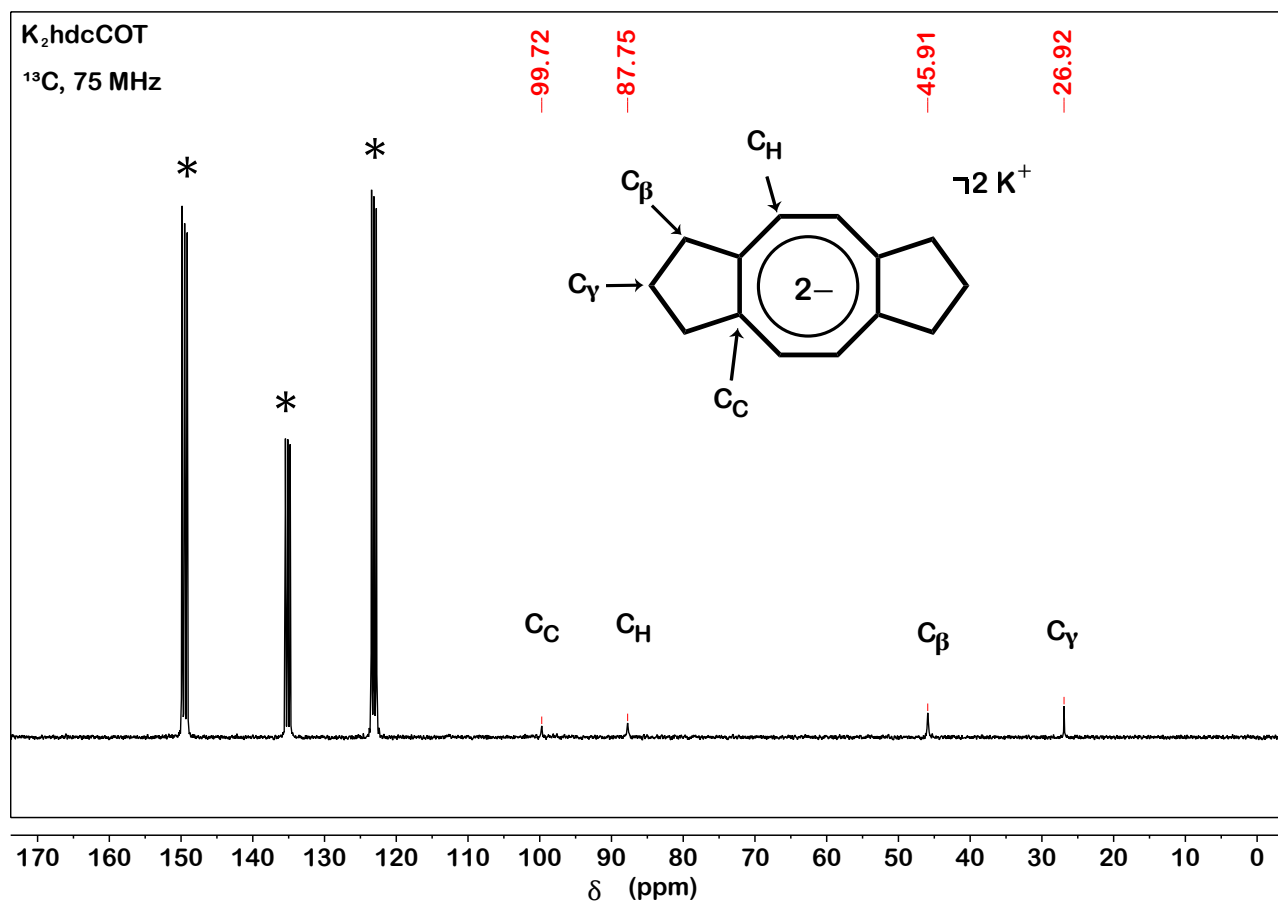**Fig. S8.** ^{1}H NMR spectrum for U(hdcCOT)$_2$. Peaks from residual C$_5$D$_4$HN are marked with an asterisk.
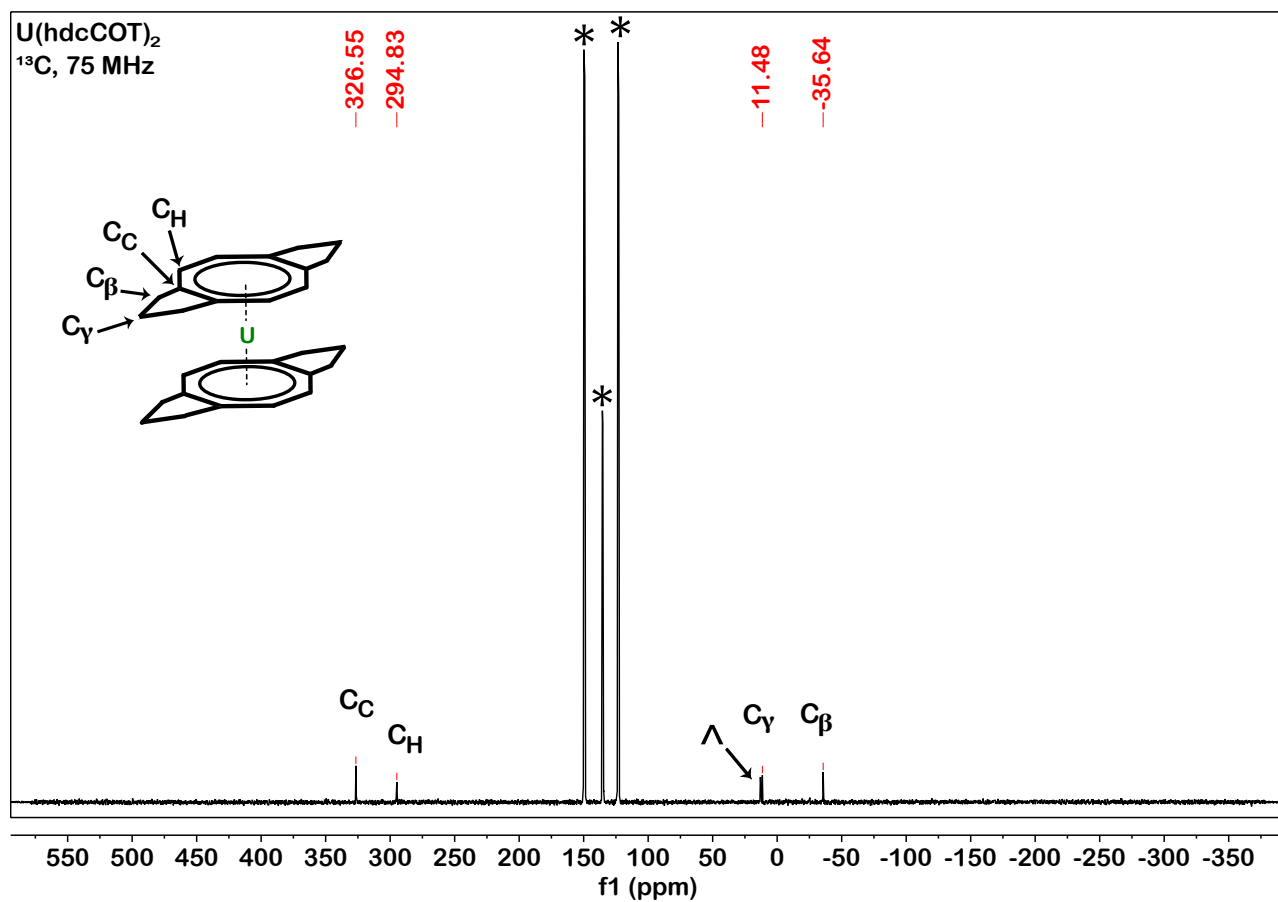
Fig. S9. $^{13}C\{^1H\}$ NMR spectrum for U(hdcCOT)$_2$. Peaks from residual C$_5$D$_4$HN are marked with an asterisk and a small peak assigned as *n*-pentane is labelled with a carat.
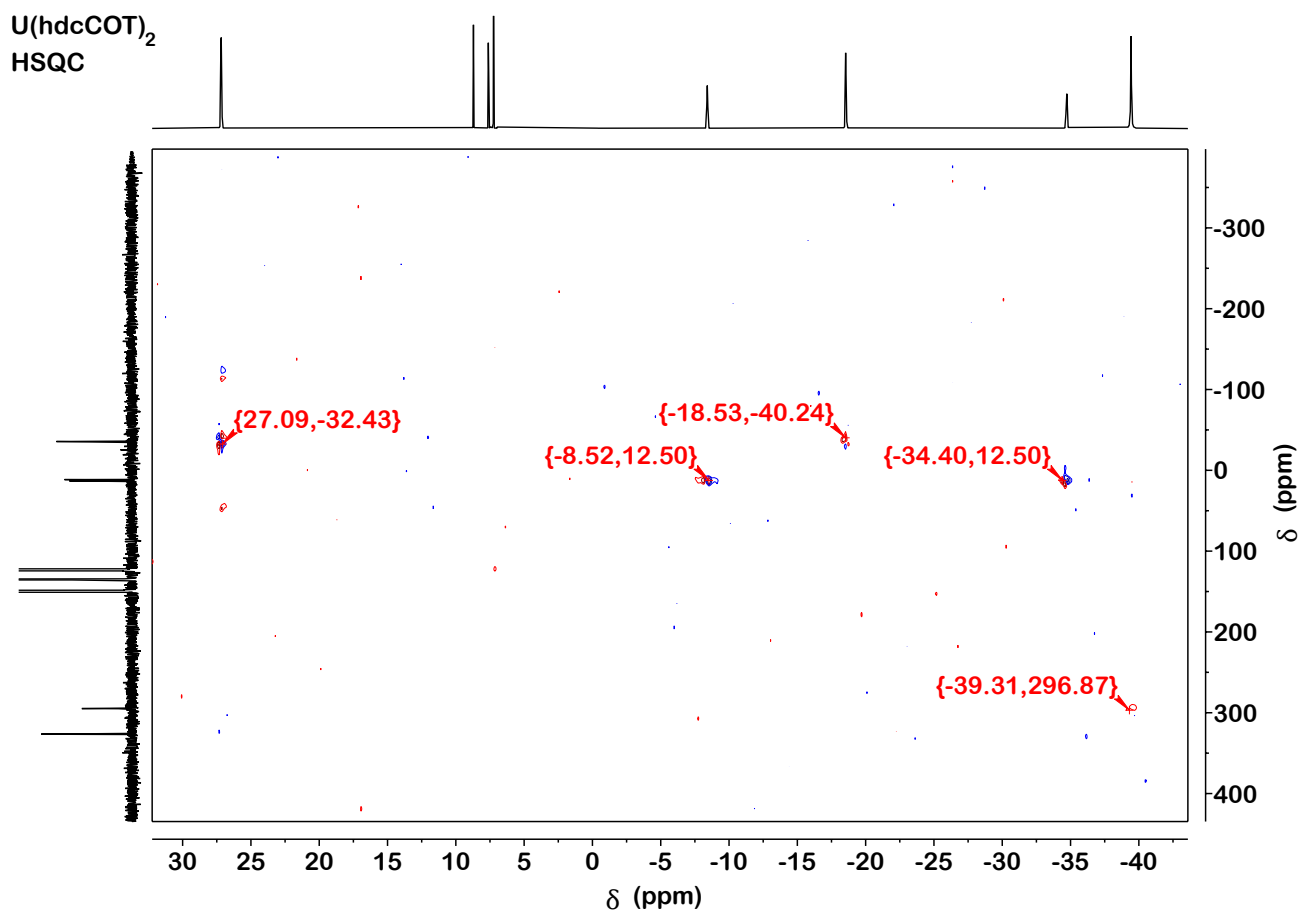
Fig. S10. $^{13}C\{^{1}H\}$-^{1}H HSQC 2D NMR spectrum for U(hdcCOT)$_2$. The ^{13}C resonance with no cross peak is assigned as the completely substituted sp^2 carbon within the [8]annulene ring. Cross peaks from residual C$_5$D$_4$HN are marked with an asterisk.
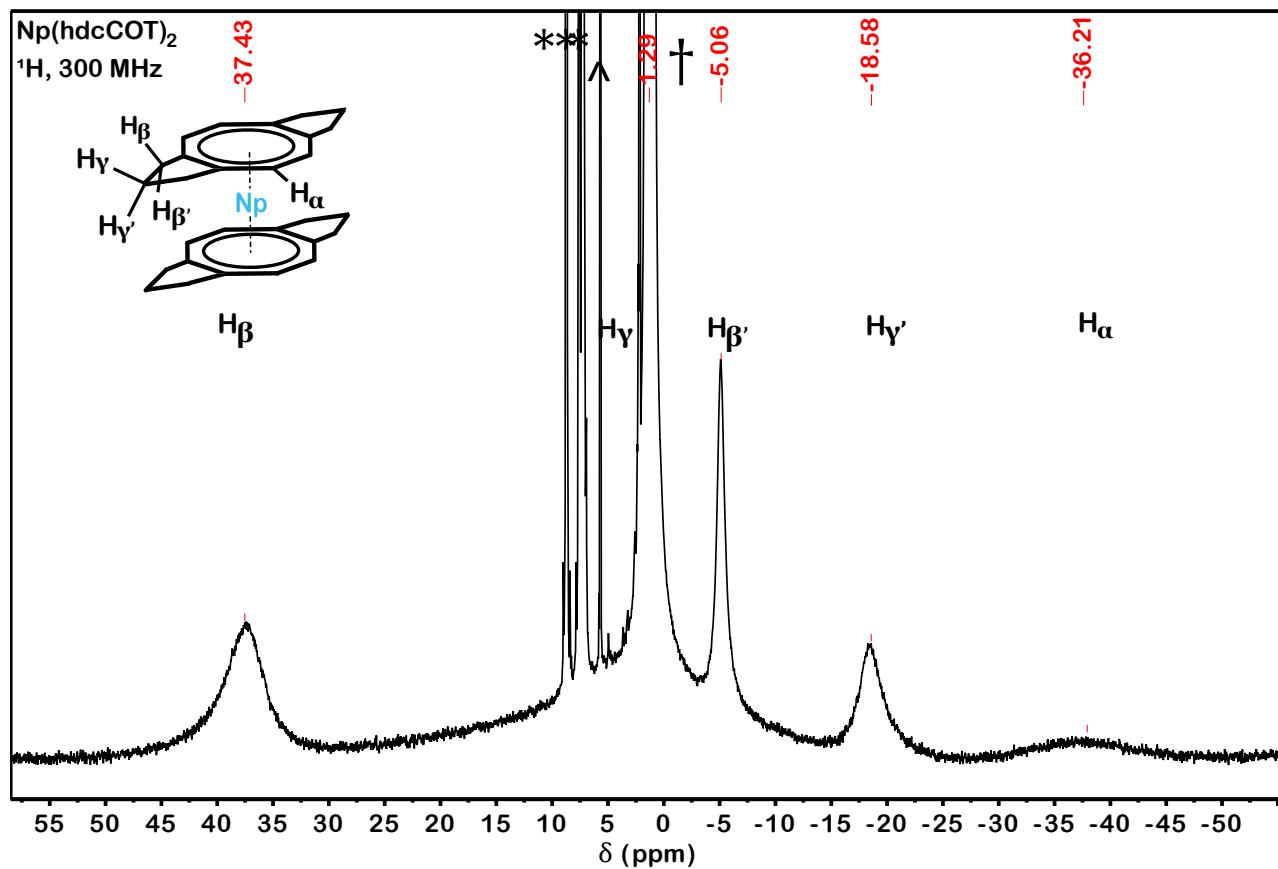
Fig. S11. ^1H NMR spectrum for Np(hdcCOT)$_2$. Peaks from residual C$_5$D$_4$HN are marked with an asterisk. Peaks from hdcCOT and *n*-pentane impurities are marked with a carat and a cross, respectively.
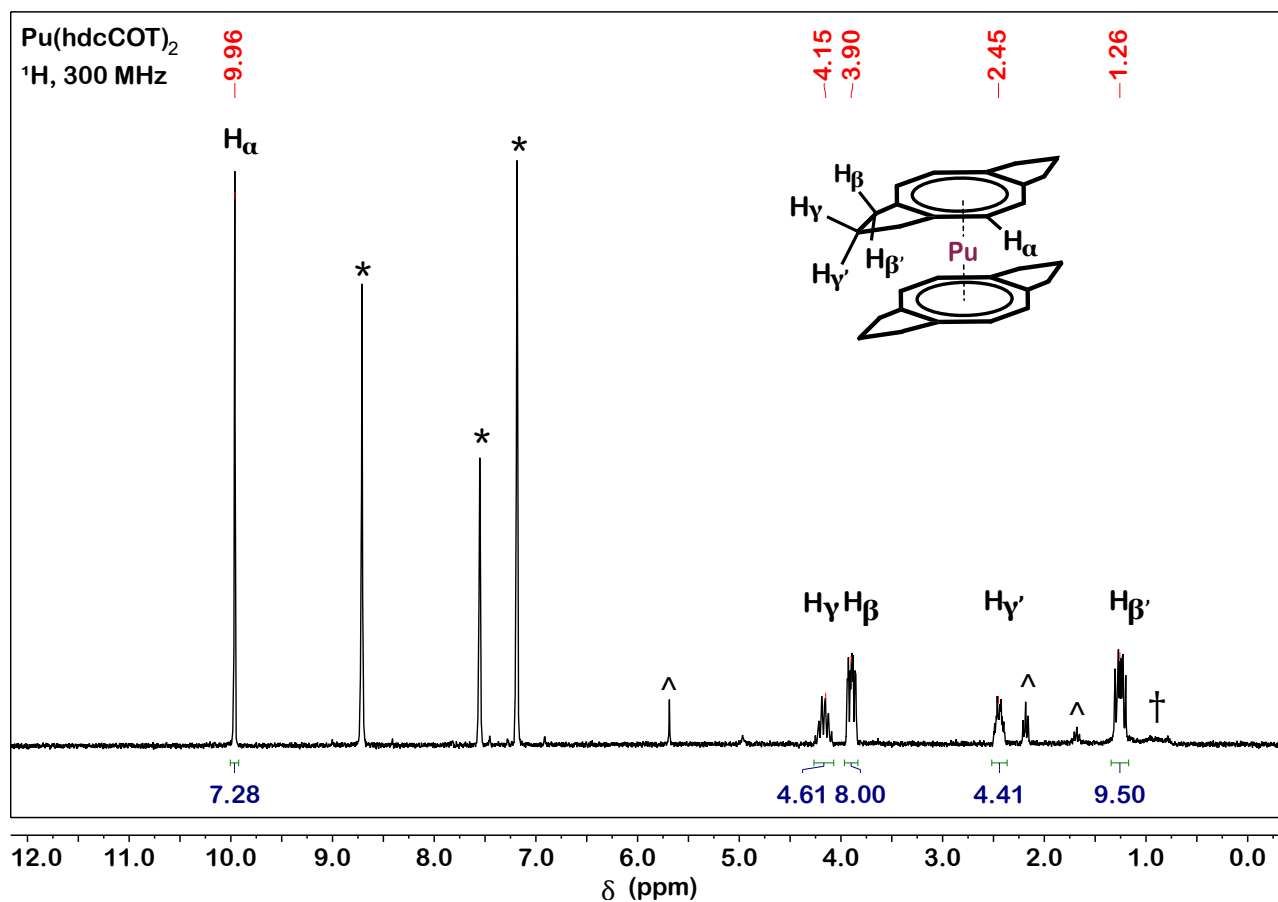
Fig. S12. ^{1}H NMR spectrum for Pu(hdcCOT)$_2$. Peaks from residual C$_5$D$_4$HN are marked with an asterisk. Peaks from hdcCOT and *n*-pentane impurities are marked with a carat and a cross, respectively.
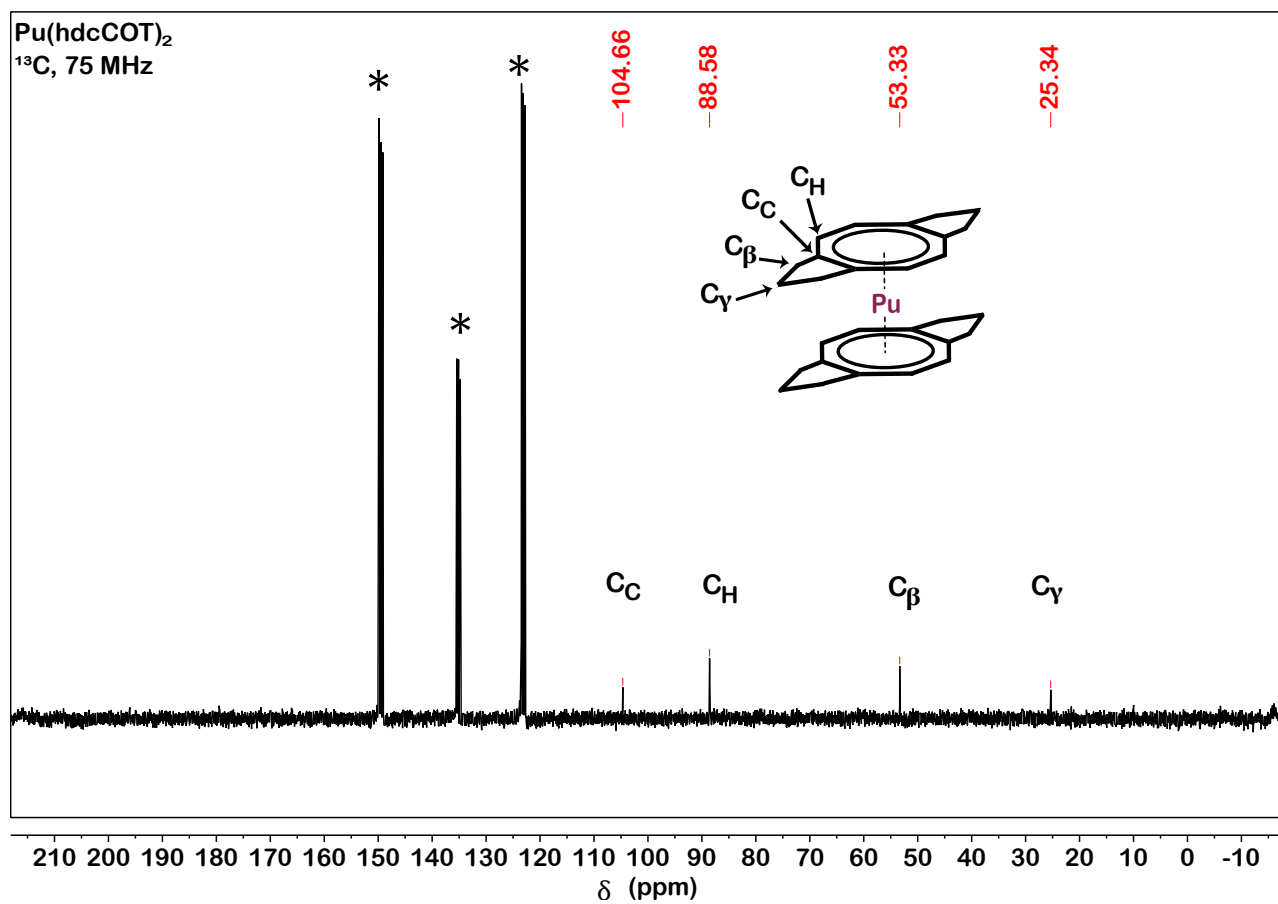
Fig. S13. $^{13}C\{^1H\}$ NMR spectrum for Pu(hdcCOT)$_2$. Peaks from residual C$_5$D$_4$HN are marked with an asterisk.
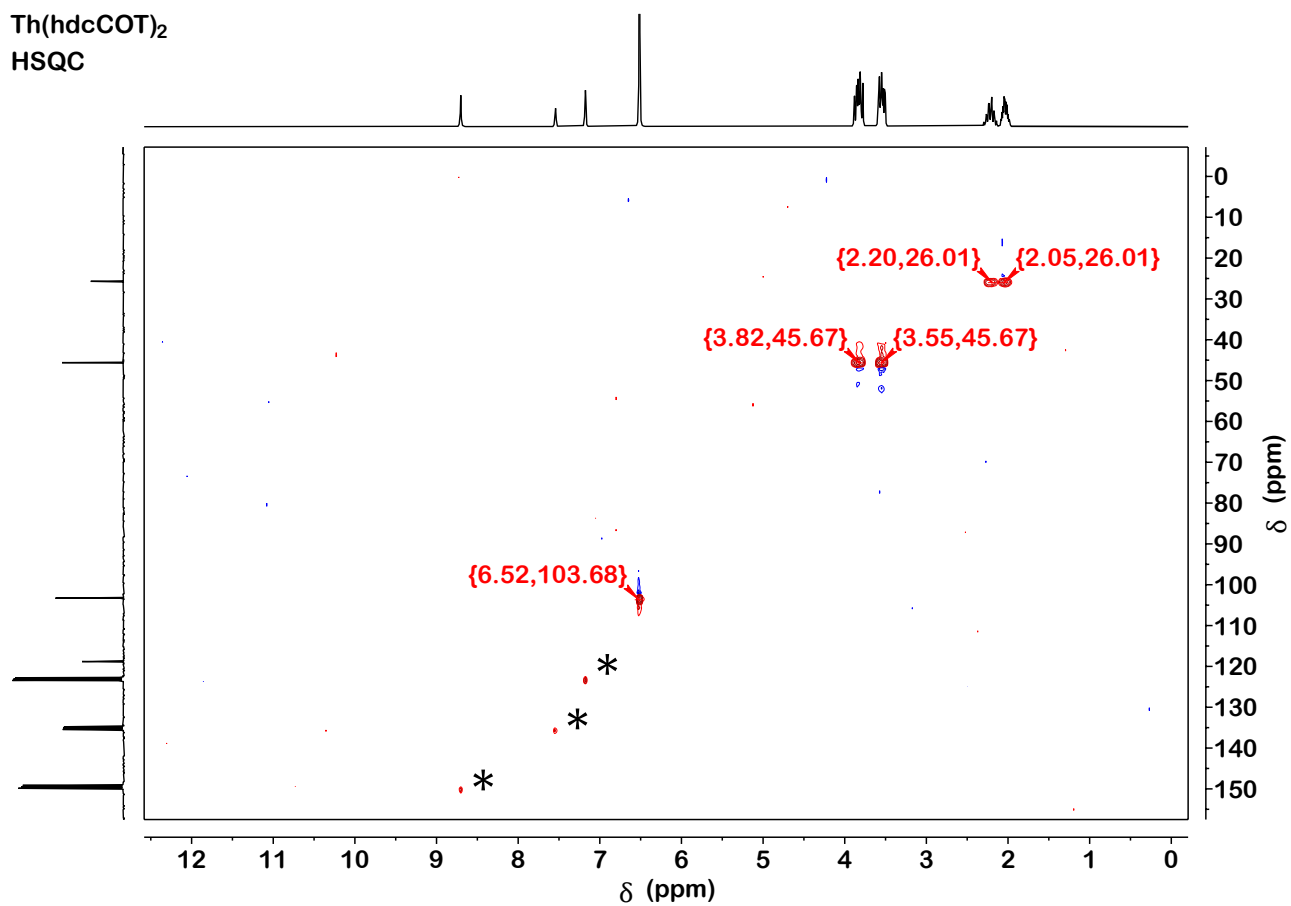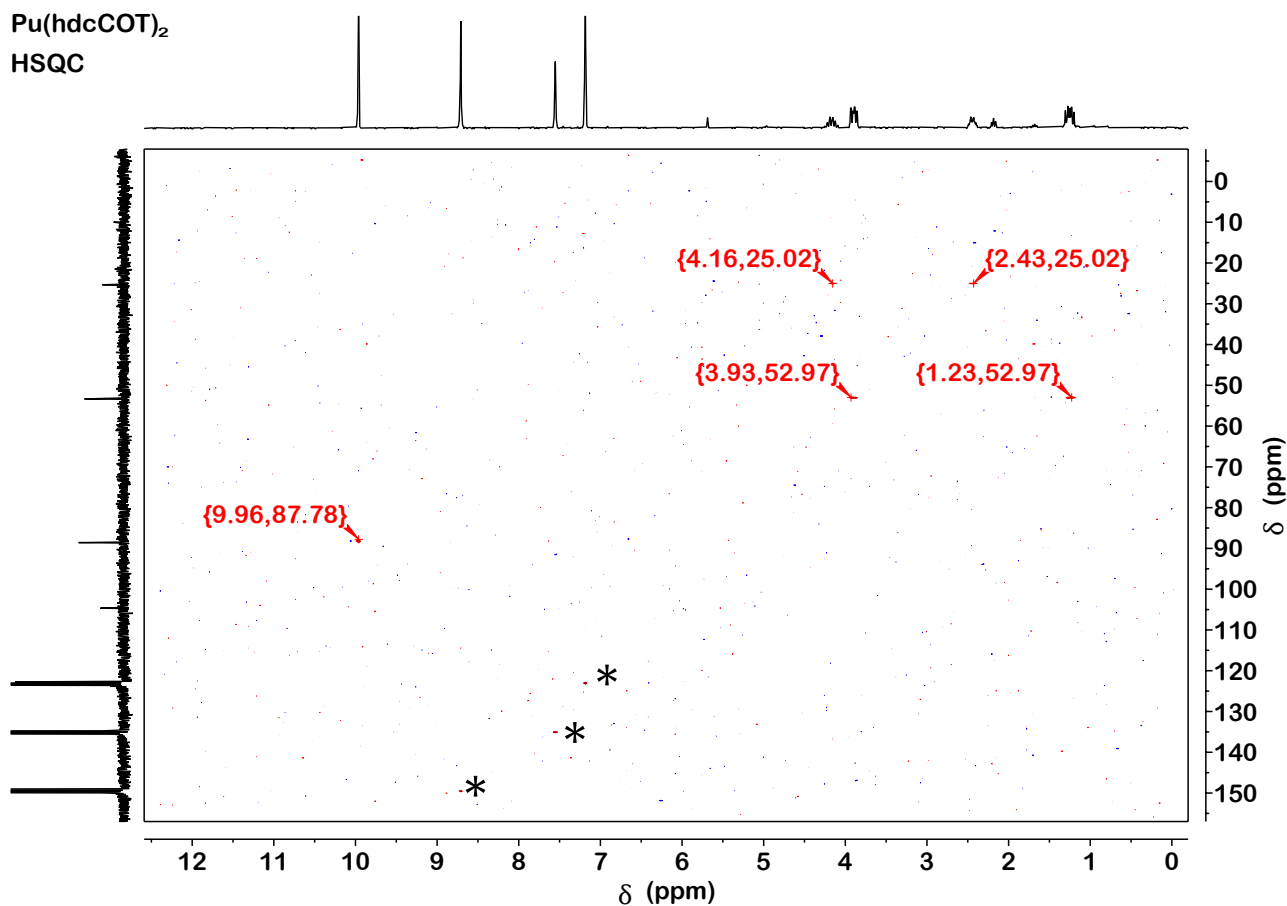
Fig. S14. $^{13}C\{^1H\}$-^1H HSQC 2D NMR spectrum for Pu(hdcCOT)$_2$. The ^{13}C resonance with no cross peak is assigned as the completely substituted sp^2 carbon within the [8]annulene ring. Cross peaks from residual C$_5$D$_4$HN are marked with an asterisk.

Table S1. Chemical shifts for the $^{13}C\{^1H\}$ resonances of K$_2$hdcCOT and M(hdcCOT)$_2$ in py-d$_5$.

Carbon Type	Chemical shift (ppm)				
	K	Th	U[†]dff	Np[‡]	Pu
C$_C$	99.72	118.8	326.6	–	104.7
C$_H$	87.75	103.3	294.8	–	88.58
C$_\beta$	45.91	45.60	−35.64	–	53.88
C$_\gamma$	28.91	25.70	11.48	–	25.34

[†] The paramagnetic contact shift for the ^{13}C resonances has an opposite effect as for in the ^1H resonances. As a result, the ring C$_C$/C$_H$ and the C$_\gamma$ carbons are shifted downfield while the C$_\beta$ carbons are shifted substantially upfield.[26–27]
[‡] No $^{13}C\{^1H\}$ resonances were observed after sweeping between ±500 ppm.

FT-IR spectra.
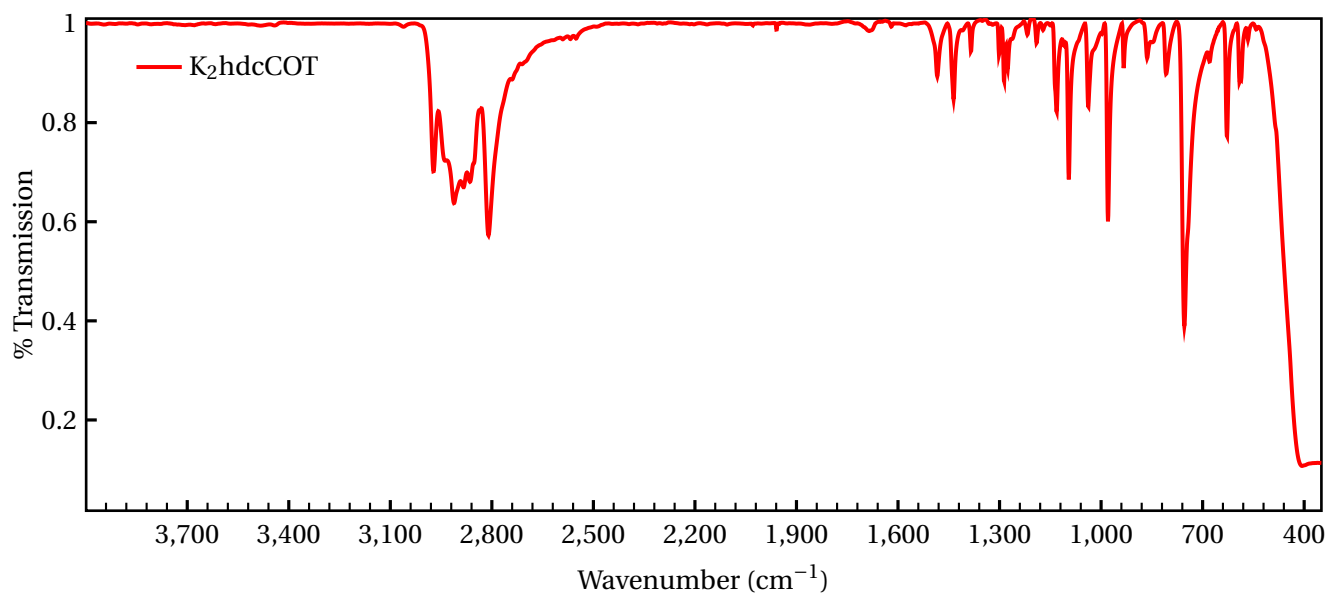
Fig. S15. FT-IR spectrum of $K_2hdcCOT$ as a Nujol mull.
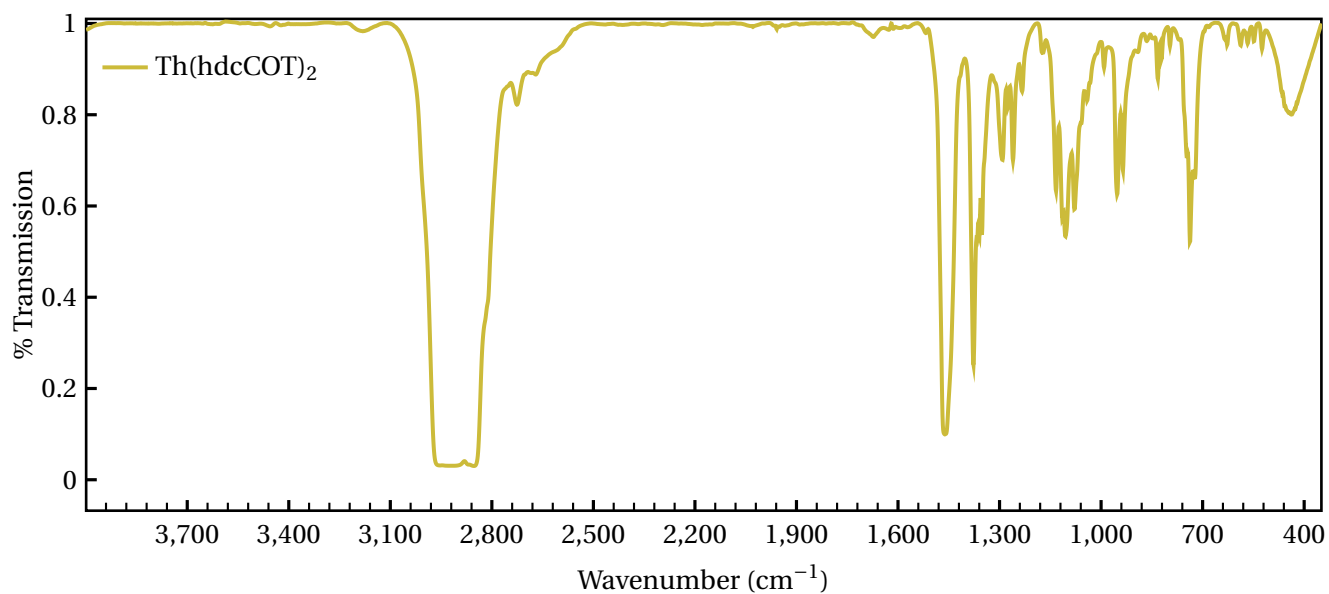
Fig. S16. FT-IR spectrum of $Th(hdcCOT)_2$ as a Nujol mull.
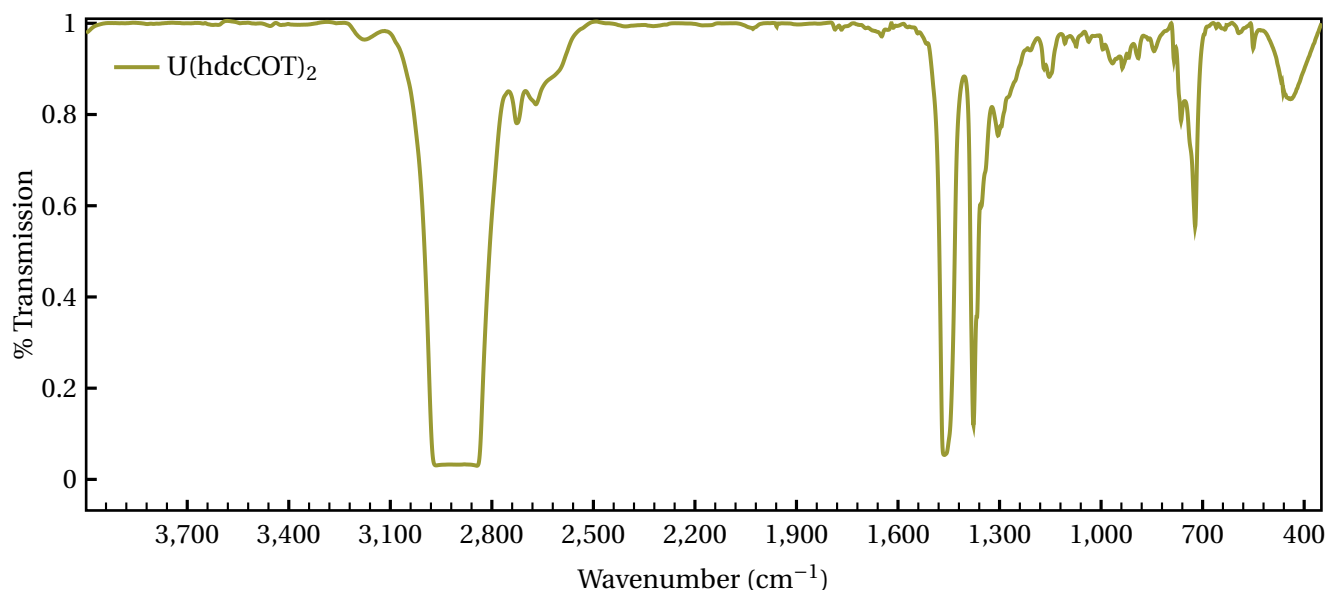
Fig. S17. FT-IR spectrum of U(hdcCOT)$_2$ as a Nujol mull.

Spherical coordinate calculations. The Cartesian coordinates tabulated below were generated from the asymmetric unit cell of the room temperature (D_{2h}) crystal structures of U(hdcCOT)$_2$ and Pu(hdcCOT)$_2$ with CrystalMaker.[19] These coordinates were then shifted and rotated so that the metal atom was centered at the origin and the three C_2 rotations were coincident with the x, y, and z axes. The spherical coordinates were then calculated using Matlab's "cart2sph" function.[28] The calculated values were then adjusted in accordance to the convention outlined in Figure S18. The pseudocontact shift was calculated according to equation (1) outlined previously.[27–29] The principal components of the magnetic susceptibility tensor are χ_x, χ_y, χ_z while θ, ϕ, and r are the spherical coordinates of of ith atom. Since U(hdcCOT)$_2$ and Pu(hdcCOT)$_2$ are symmetric, $\chi_x = \chi_y$; the second term is zero and the sign of the first term is dictated by θ.

$$\delta_{\text{pseudocontact}} = \left(\frac{\chi_z - \frac{1}{2}\left(\chi_x - \chi_y\right)}{3} \right)\left(\frac{3\cos^2\theta - 1}{r}\right) + \left(\frac{\chi_x - \chi_y}{2}\right)\left(\frac{\sin^2\theta\cos 2\phi}{r^3}\right) \tag{1}$$
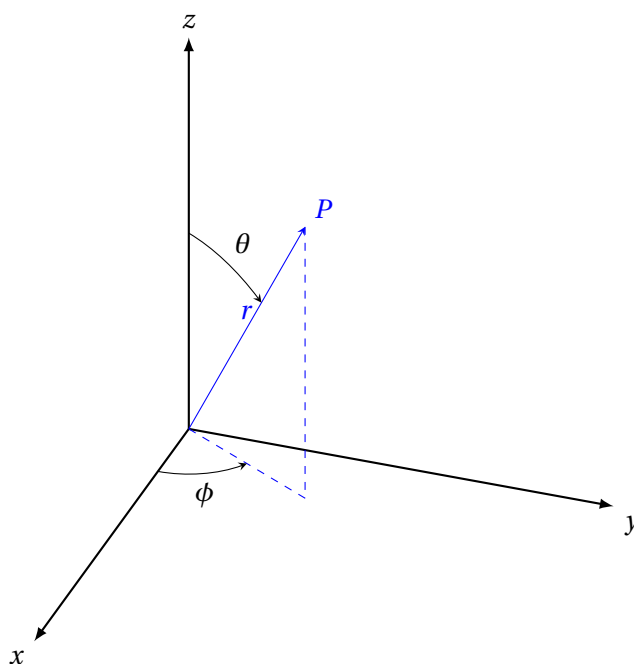
Fig. S18. Definitions for θ and ϕ to represent point P, which is the ith atom, used in converting the atomic Cartesian coordinates into spherical coordinates. The length of the vector from the origin to P defines r.

Table S2. Atomic and spherical coordinates for U(hdcCOT)$_2$. Hydrogens highlighted are *exo*. Since all of the M(hdcCOT)$_2$ complexes presented here are isostructural, Np(hdcCOT)$_2$ and Pu(hdcCOT)$_2$ will follow a similar pattern.

Atom	x	y	z	r (Å)	θ (°)	ϕ (°)
U1	0.000	0.000	0.000	0.000	90.00	0.000
C1	1.670	−0.706	1.960	2.670	42.77	337.1
C2	1.696	0.709	1.949	2.680	43.32	22.688
C3	0.739	1.699	1.876	2.636	44.65	66.490
C4	−0.684	1.739	1.860	2.637	45.14	111.5
C5	−1.695	0.749	1.938	2.682	43.72	156.2
C6	−1.710	−0.664	1.967	2.689	43.00	201.2
C7	−0.763	−1.649	1.884	2.617	43.96	245.2
C8	0.635	−1.673	1.906	2.615	43.19	290.8
C9	3.128	−1.236	2.010	3.918	59.14	338.4
C10	4.023	−0.008	2.067	4.523	62.80	359.9
C11	3.171	1.208	1.932	3.905	60.35	20.855
C12	−3.137	1.229	2.006	3.921	59.23	158.6
C13	−3.936	−0.026	1.904	4.372	64.18	180.4
C14	−3.114	−1.182	2.028	3.899	58.66	200.8
H3	1.115	2.548	1.823	3.325	56.76	66.363
H4	−1.024	2.601	1.782	3.315	57.48	111.5
H7	−1.135	−2.497	1.792	3.277	56.84	245.6
H8	0.969	−2.541	1.879	3.305	55.36	290.9
H9A	3.262	−1.792	2.789	4.650	53.15	331.2
H9B	3.325	−1.757	1.214	3.952	72.11	332.1
H10B	4.497	0.013	2.915	5.359	57.04	0.160
H10A	4.677	−0.039	1.354	4.869	73.86	359.5

H11B	3.332	1.823	2.665	4.640	54.94	28.681
H11A	3.365	1.667	1.097	3.912	73.71	26.358
H12A	−3.313	1.690	2.839	4.679	52.64	153.0
H12B	−3.337	1.828	1.266	4.010	71.60	151.3
H13B	−4.606	−0.037	2.606	5.293	60.50	180.5
H13A	−4.395	−0.050	1.052	4.519	76.55	180.6
H14B	−3.278	−1.631	2.870	4.652	51.91	206.5
H14A	−3.283	−1.800	1.301	3.964	70.84	208.7
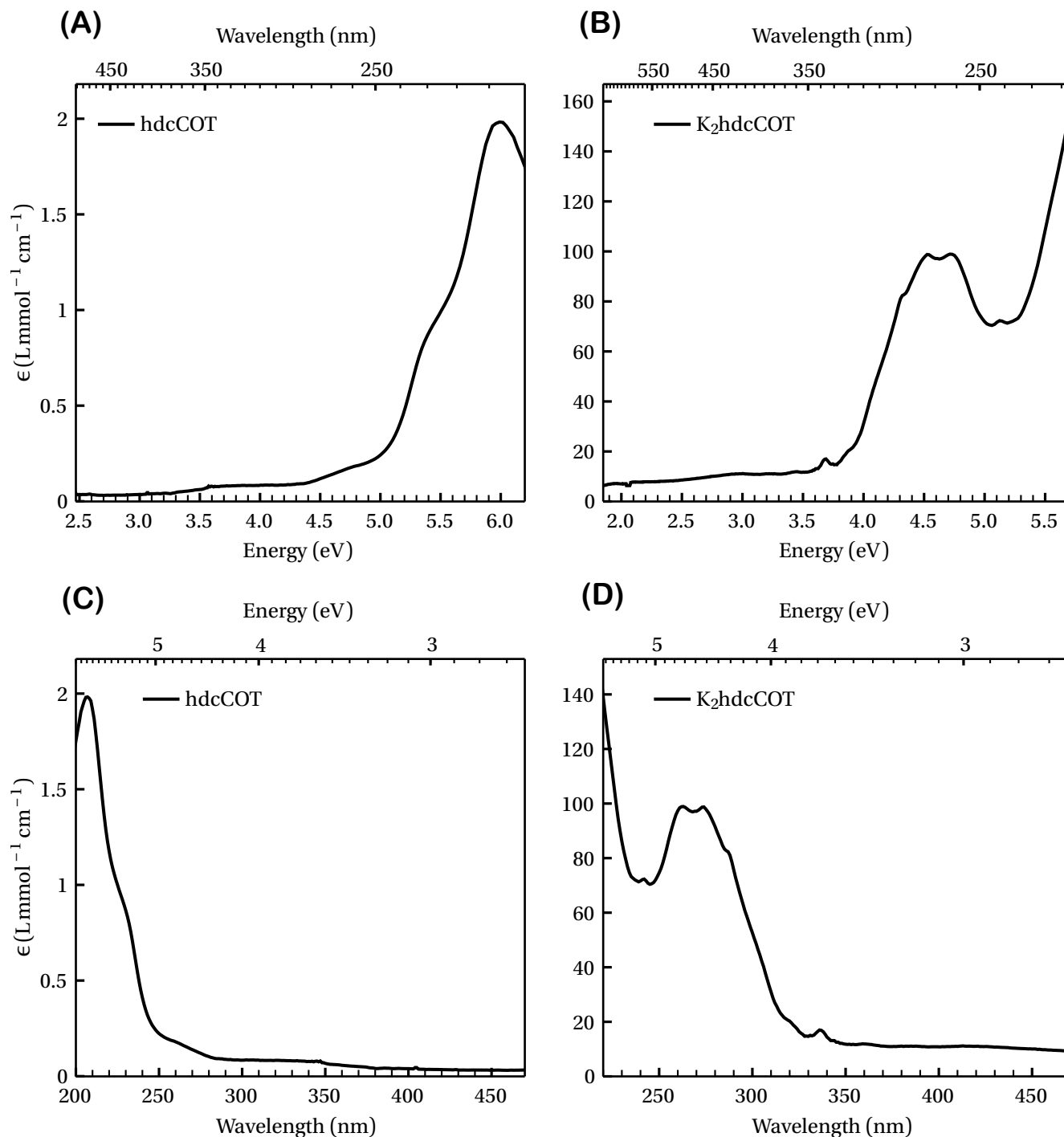
Fig. S19. (A) Normalized UV-Vis-NIR spectrum for hdcCOT collected in *n*-hexane. **(B)** Normalized UV-Vis-NIR spectrum of K_2hdcCOT collected in THF. **(C)** and **(D)** are replots of **(A)** and **(B)**, respectively, with the primary axis listed in wavelength and the secondary axis in energy. For **(C)** and **(D)**, the minor ticks of the secondary axis correspond to a 0.1 eV change. The intensities in all four plots have been normalized to absorptivities ($L\,mmol^{-1}\,cm^{-1}$).
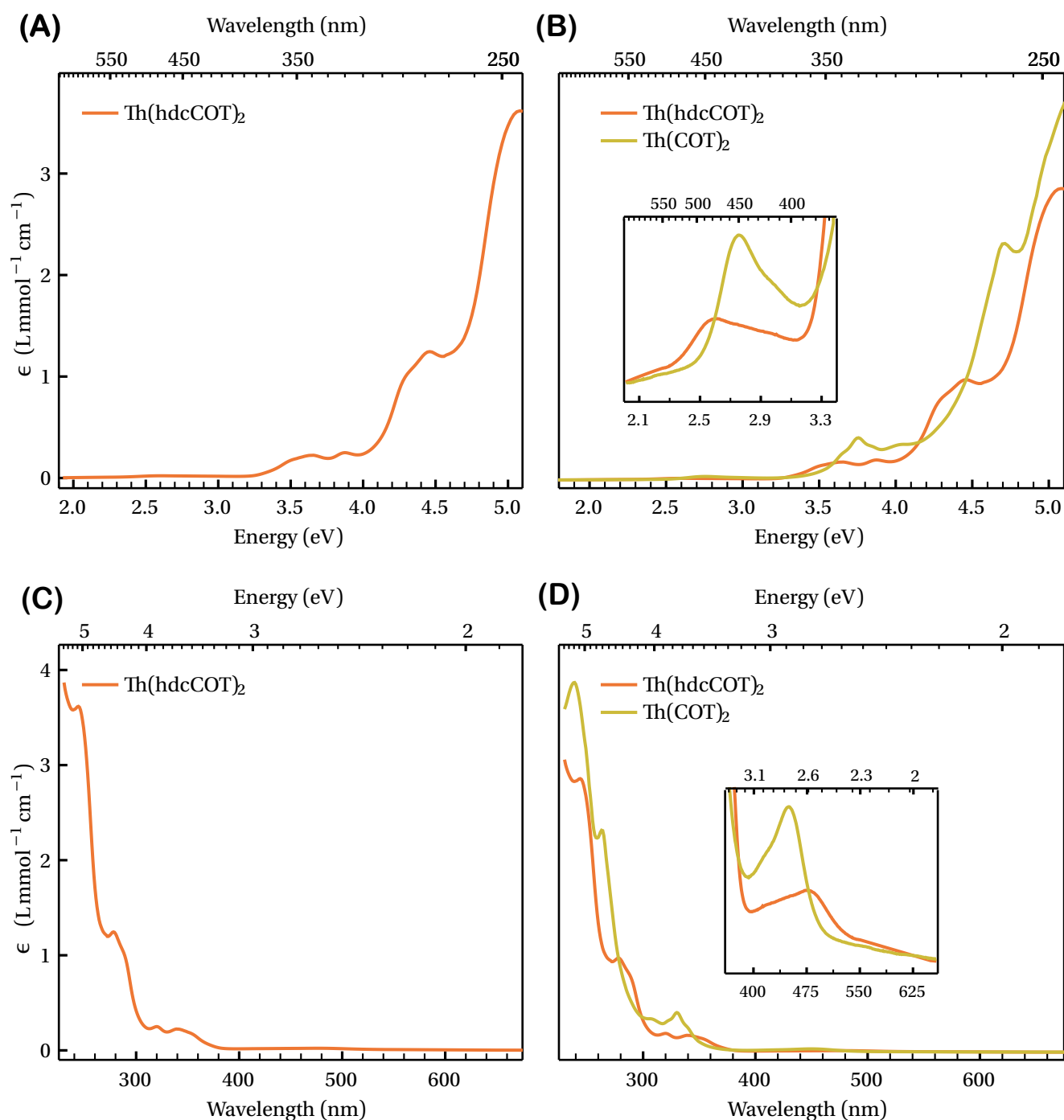
Fig. S20. (A) UV-Vis-NIR spectrum for Th(hdcCOT)$_2$ collected in THF. **(B)** Comparison of Th(hdcCOT)$_2$ and Th(COT)$_2$. Each minor tick of the secondary axis corresponds to a change of 10 nm. **(C)** and **(D)** are replots of **(A)** and **(B)**, respectively, with the primary axis listed in wavelength and the secondary axis in energy. For **(C)** and **(D)**, the minor ticks of the secondary axis correspond to a 0.1 eV change. The inset plot for **(B)** and **(D)** emphasize the region plotted in the main manuscript. The intensities in all four plots have been normalized to absorptivities ($\mathrm{Lmmol^{-1}\,cm^{-1}}$).
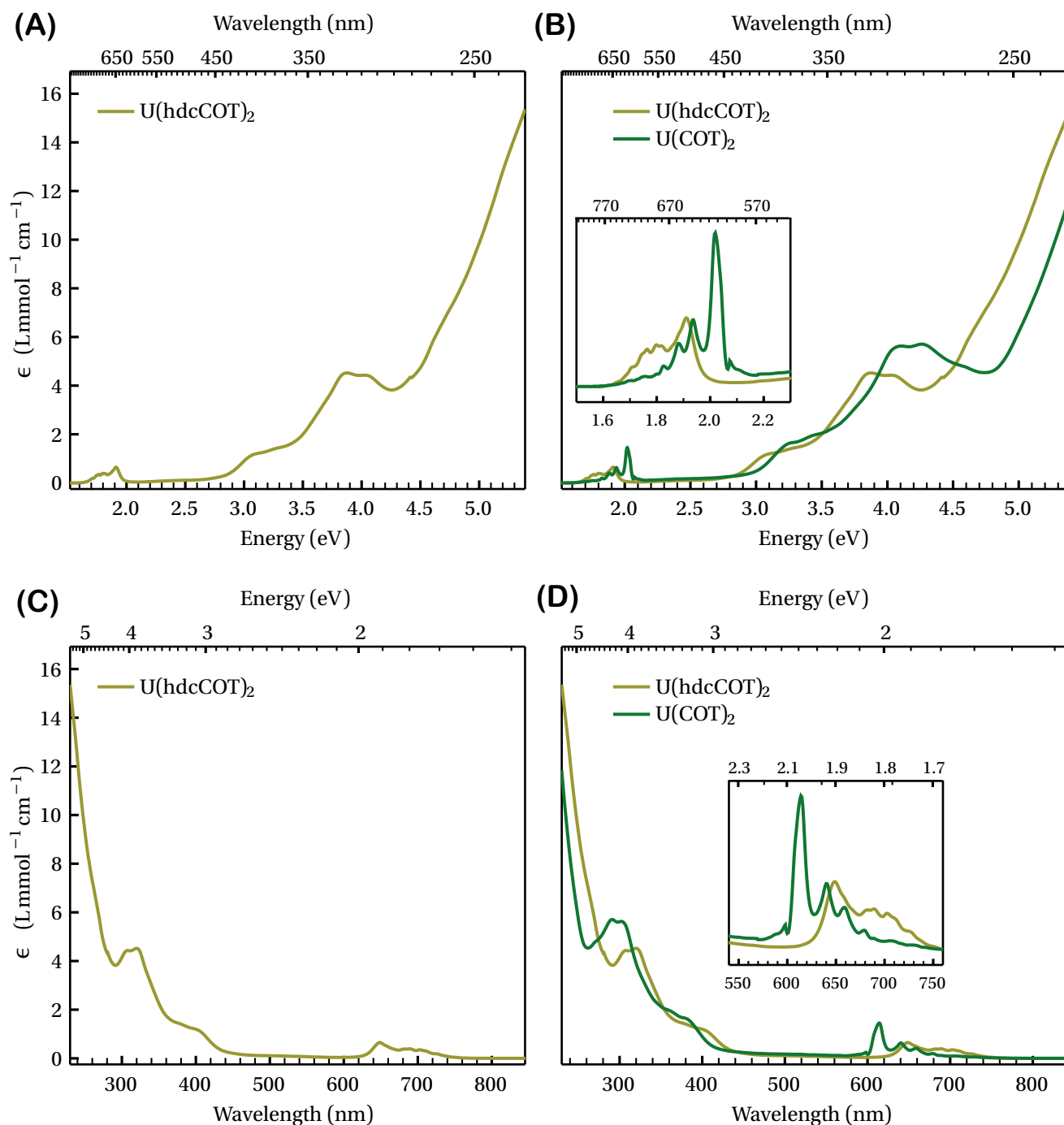
Fig. S21. (A) UV-Vis-NIR spectrum for U(hdcCOT)$_2$ collected in THF. **(B)** Comparison of U(hdcCOT)$_2$ and U(COT)$_2$ windowed approximately in the visible region. The primary axis is listed here in energy while the secondary axis is listed in wavelength. Each minor tick of the secondary axis corresponds to a change of 10 nm. **(C)** and **(D)** are replots of **(A)** and **(B)**, respectively, with the primary axis listed in wavelength and the secondary axis in energy. For **(C)** and **(D)**, the minor ticks of the secondary axis correspond to a 0.1 eV change. The intensities in all four plots have been normalized to absorptivities (Lmmol^{-1}cm^{-1}).
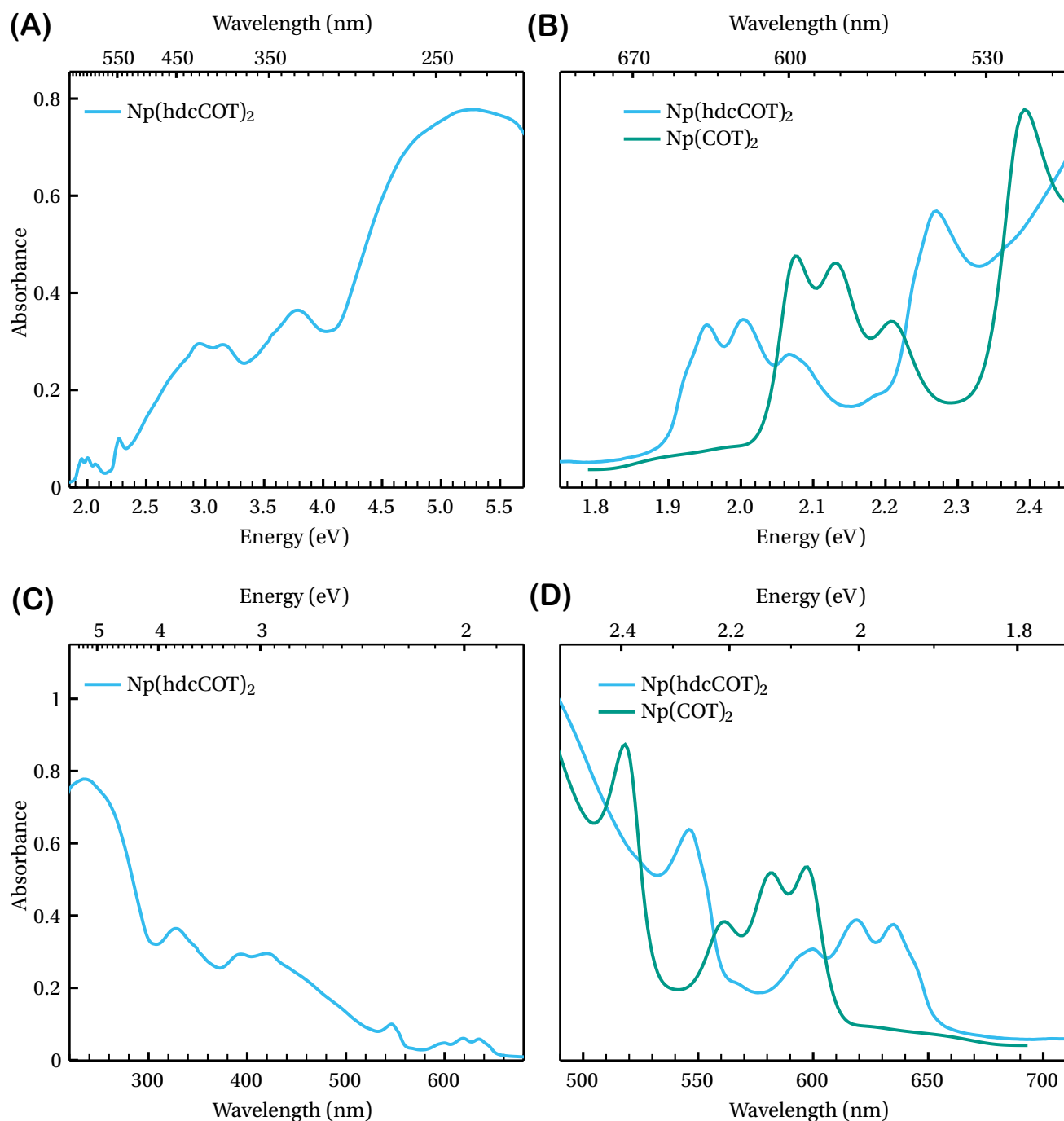
Fig. S22. (A) UV-Vis-NIR spectrum for Np(hdcCOT)$_2$ collected in *n*-hexane. **(B)** Comparison of Np(hdcCOT)$_2$ and Np(COT)$_2$ windowed on the region corresponding to what was reported for Np(COT)$_2$.[30] These data were digitized from the original publication. The primary axis is listed here in energy while the secondary axis is listed in wavelength. Each minor tick of the secondary axis corresponds to a change of 10 nm. **(C)** and **(D)** are replots of **(A)** and **(B)**, respectively, with the primary axis listed in wavelength and the secondary axis in energy. For **(C)** and **(D)**, the minor ticks of the secondary axis correspond to a 0.1 eV change. The intensities in **(B)** and **(D)** are arbitrary and have been scaled for best visual clarity. The raw absorption intensity for the Np(hdcCOT)$_2$ are presented for accuracy in **(A)** and **(C)** with no change in scaling.
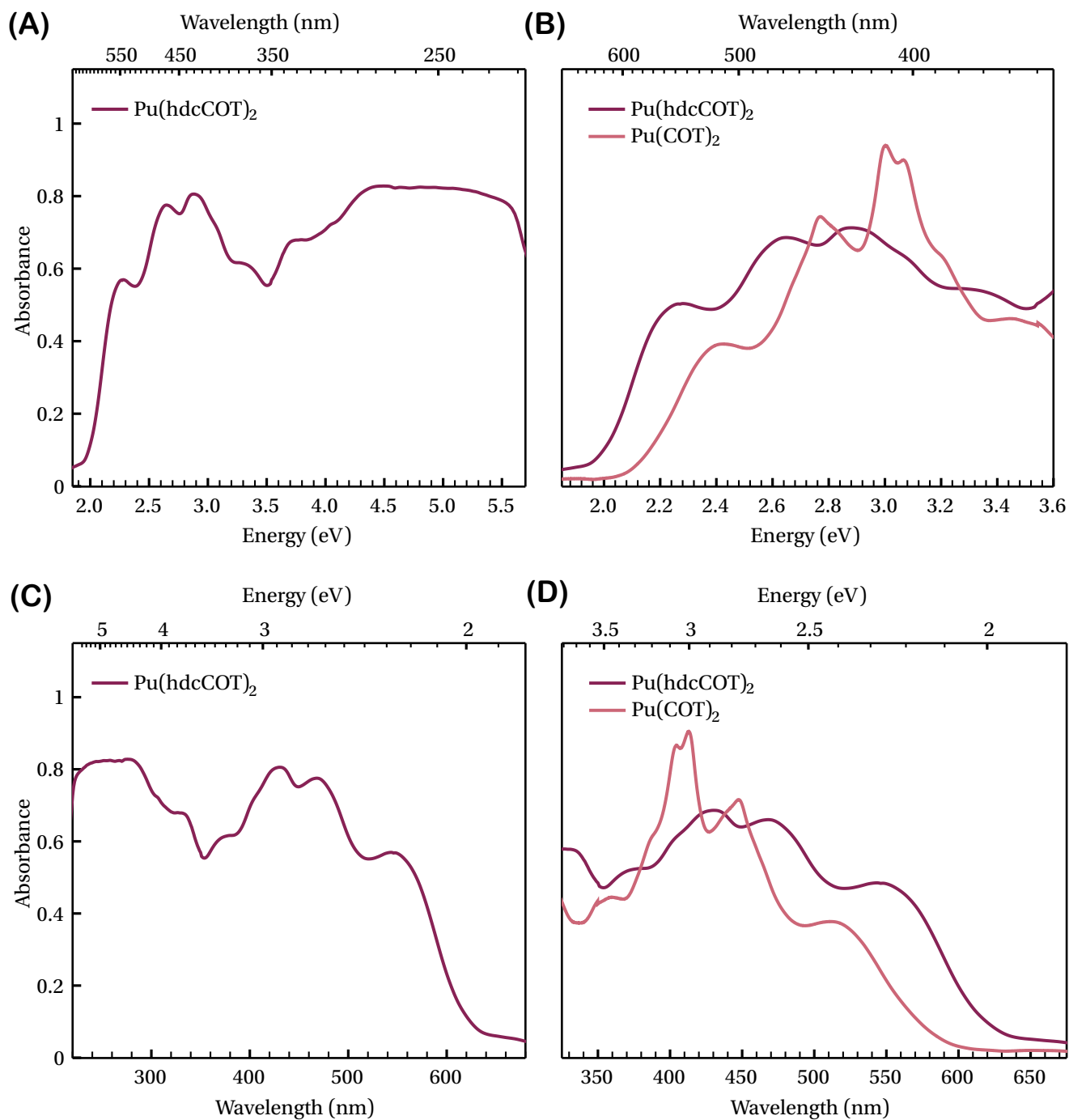
Fig. S23. A. UV-Vis-NIR spectrum for Pu(hdcCOT)$_2$ collected in *n*-hexane. **B.** Comparison of Pu(hdcCOT)$_2$ and Pu(COT)$_2$ windowed primarily in the visible region. Note that The data for Pu((COT)$_2$ were collected in PhMe. The primary (bottom) axis is listed here in energy while the secondary axis (top) is listed in wavelength. Each minor tick of the secondary axis corresponds to a change of 10 nm. The intensity is arbitrary and has been scaled for best visual clarity. The raw absorption intensity for the Pu(hdcCOT)$_2$ are presented in **(A)** with no change in scaling.

5. Crystallography

Renders and selected bond metrics.

hdcCOT

Fig. S24. X-ray crystal structure of hdcCOT at 100 K with thermal ellipsoids plotted at 50% probability. H atoms were removed for clarity.

Table S3. Table of bond lengths for hdcCOT at 100 K.

Bond ($C = C$)	Distance (Å)	Bond ($C - C$)	Distance (Å)
C1 − C2	1.337(2)	C2 − C3	1.470(2)
C3 − C4	1.329(2)	C4 − C5	1.463(2)
C5 − C6	1.340(2)	C6 − C7	1.471(2)
C7 − C8	1.330(2)	C8 − C1	1.466(2)
$\langle C = C \rangle$	1.334(5)		
$\langle C - C \rangle$	1.468(4)		

Th(hdcCOT)₂.
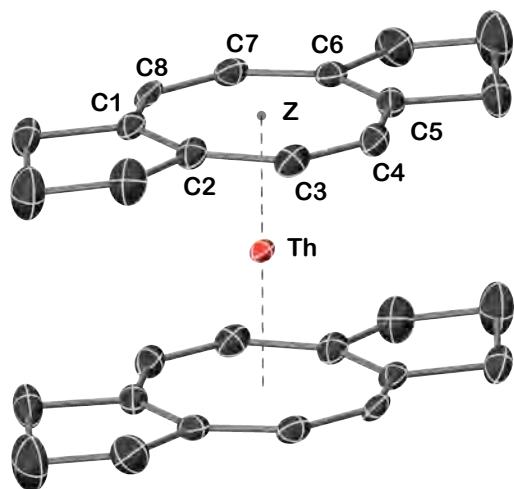
Fig. S25. X-ray crystal structure of Th(hdcCOT)₂ at 150 K with thermal ellipsoids plotted at 50% probability. H atoms were removed for clarity.

Table S4. Table of bond lengths for Th(hdcCOT)$_2$ at 150 K. Z labels the [8]annulene ring centroid. C_C and C_H refer to the two types of [8]annulene carbons.

Bond (C_C)	Distance (Å)	Bond (C_H)	Distance (Å)
Th − C1	2.745(4)	Th − C3	2.709(4)
Th − C2	2.754(3)	Th − C4	2.709(4)
Th − C5	2.747(3)	Th − C7	2.709(5)
Th − C6	2.745(3)	Th − C8	2.697(6)
$\langle Th - C_C \rangle$	2.748(4)		
$\langle Th - C_H \rangle$	2.706(5)		
$\langle Th - C \rangle$	2.73(2)		
$\langle Th \cdots Z \rangle$	2.0062(1)		

Fig. S26. X-ray crystal structure of Th(hdcCOT)$_2$ at 293 K with thermal ellipsoids plotted at 50% probability. H atoms were removed for clarity.

Table S5. Table of bond lengths for Th(hdcCOT)$_2$ at 293 K. Z labels the [8]annulene ring centroid. C_C and C_H refer to the two types of [8]annulene carbons.

Bond (C_C)	Distance (Å)	Bond (C_H)	Distance (Å)
Th – C1	2.747(4)	Th – C3	2.704(5)
Th – C2	2.746(5)	Th – C4	2.702(4)
Th – C5	2.751(4)	Th – C7	2.708(4)
Th – C6	2.753(4)	Th – C8	2.708(4)
$\langle$Th – $C_C\rangle$	2.749(3)		
$\langle$Th – $C_H\rangle$	2.706(3)		
$\langle$Th – C$\rangle$	2.73(2)		
$\langle$Th$\cdots$Z$\rangle$	2.013(2)		

U(hdcCOT)$_2$.

Fig. S27. X-ray crystal structure of U(hdcCOT)$_2$ at 100 K with thermal ellipsoids plotted at 50% probability. H atoms were removed for clarity.

Table S6. Table of bond lengths for U(hdcCOT)$_2$ at 100 K. Z labels the [8]annulene ring centroid. C_C and C_H refer to the two types of [8]annulene carbons.

Bond (C_C)	Distance (Å)	Bond (C_H)	Distance (Å)
U – C1	2.706(3)	U – C3	2.644(3)
U – C2	2.698(3)	U – C4	2.644(3)
U – C5	2.702(3)	U – C7	2.650(3)
U – C6	2.697(3)	U – C8	2.650(3)
$\langle$U – $C_C\rangle$	2.701(4)		
$\langle$U – $C_H\rangle$	2.647(3)		
$\langle$U – C$\rangle$	2.70(2)		
$\langle$U$\cdots$Z$\rangle$	1.932(1)		

U(hdcCOT)₂.
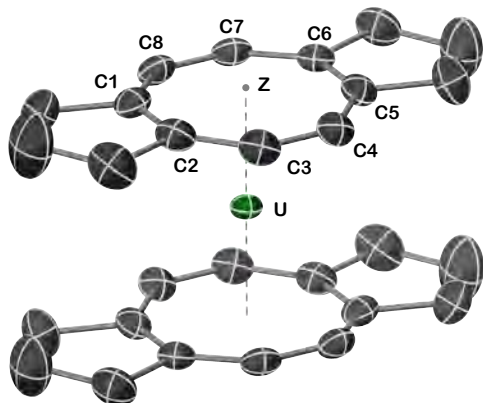
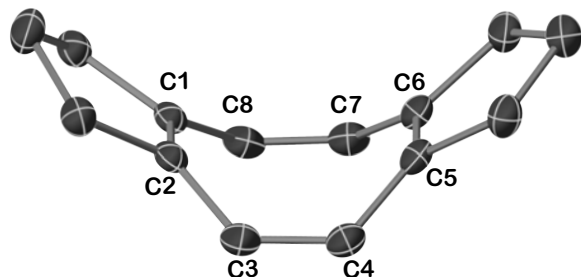**Fig. S28.** X-ray crystal structure of U(hdcCOT)$_2$ at 293 K with thermal ellipsoids plotted at 50% probability. H atoms were removed for clarity.

Table S7. Table of bond lengths for U(hdcCOT)$_2$ at 293 K. Z labels the [8]annulene ring centroid. C_C and C_H refer to the two types of [8]annulene carbons.

| Bond (C_C)	Distance (Å)	Bond (C_H)	Distance (Å)
U – C1	2.699(3)	U – C3	2.651(2)
U – C2	2.699(3)	U – C4	2.649(3)
U – C5	2.697(3)	U – C7	2.644(4)
U – C6	2.695(4)	U – C8	2.647(3)
$\langle$U – $C_C\rangle$	2.698(2)		
$\langle$U – $C_H\rangle$	2.648(3)		
$\langle$U – C$\rangle$	2.67(3)		
$\langle$U$\cdots$Z$\rangle$	1.939(1)		

Np(hdcCOT)₂
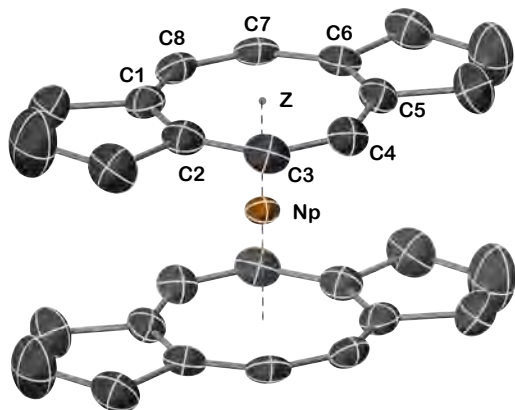
Fig. S29. X-ray crystal structure of Np(hdcCOT)$_2$ at 293 K with thermal ellipsoids plotted at 50% probability. H atoms were removed for clarity.

Table S8. Table of bond lengths for Np(hdcCOT)$_2$ at 293 K. Z labels the [8]annulene ring centroid. C_C and C_H refer to the two types of [8]annulene carbons.

Bond (C_C)	Distance (Å)	Bond (C_H)	Distance (Å)
Np – C1	2.689(2)	Np – C3	2.641(2)
Np – C2	2.691(3)	Np – C4	2.644(3)
Np – C5	2.692(3)	Np – C7	2.635(3)
Np – C6	2.687(3)	Np – C8	2.638(2)
$\langle$Np – $C_C\rangle$	2.690(2)		
$\langle$Np – $C_H\rangle$	2.640(3)		
$\langle$Np – C$\rangle$	2.67(3)		
$\langle$Np$\cdots$Z$\rangle$	1.9286(9)		

Pu(hdcCOT)₂.
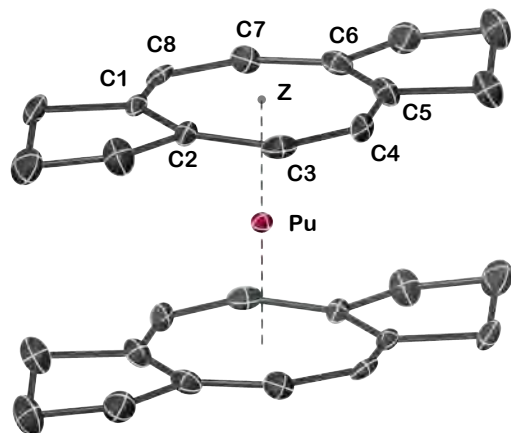
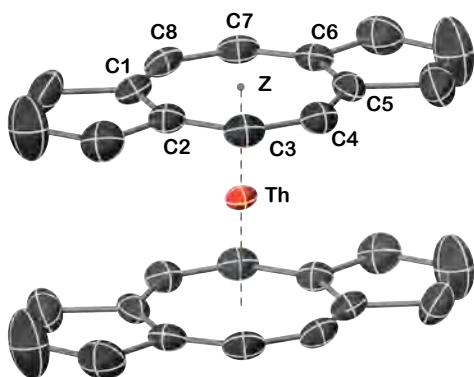**Fig. S30.** X-ray crystal structure of Pu(hdcCOT)₂ at 100 K with thermal ellipsoids plotted at 50% probability. H atoms were removed for clarity.

Table S9. Table of bond lengths for Pu(hdcCOT)₂ at 100 K. Z labels the [8]annulene ring centroid. C_C and C_H refer to the two types of [8]annulene carbons.

Bond (C_C)	Distance (Å)	Bond (C_H)	Distance (Å)
Pu – C1	2.681(5)	Pu – C3	2.631(7)
Pu – C2	2.679(5)	Pu – C4	2.641(7)
Pu – C5	2.684(5)	Pu – C7	2.62(1)
Pu – C6	2.683(6)	Pu – C8	2.650(9)
⟨Pu – C_C⟩	2.682(1)		
⟨Pu – C_H⟩	2.64(1)		
⟨Pu – C⟩	2.66(3)		
⟨Pu···Z⟩	1.912(9)		

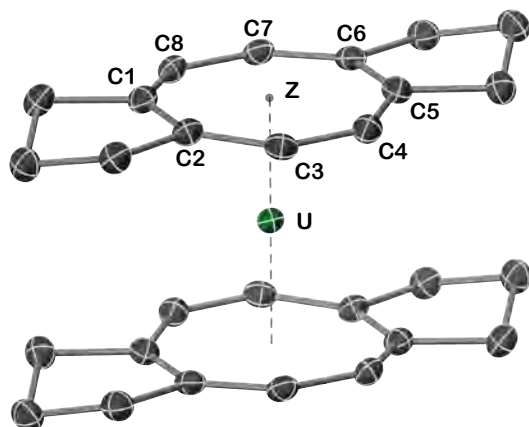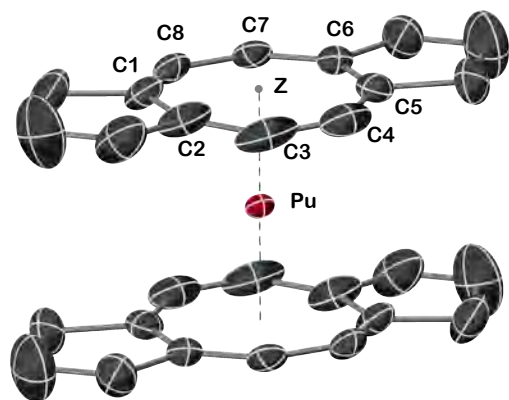**Fig. S31.** X-ray crystal structure of Pu(hdcCOT)₂ at 293 K with thermal ellipsoids plotted at 50% probability. H atoms were removed for clarity.

Table S10. Table of bond lengths for Pu(hdcCOT)₂ at 293 K. Z labels the [8]annulene ring centroid. C_C and C_H refer to the two types of [8]annulene carbons.

Bond (C_C)	Distance (Å)	Bond (C_H)	Distance (Å)
Pu – C1	2.682(9)	Pu – C3	2.62(2)
Pu – C2	2.69(1)	Pu – C4	2.615(9)
Pu – C5	2.670(8)	Pu – C7	2.636(6)
Pu – C6	2.680(8)	Pu – C8	2.637(7)
⟨Pu – C_C⟩	2.681(7)		
⟨Pu – C_H⟩	2.63(1)		
⟨Pu – C⟩	2.65(3)		
⟨Pu···Z⟩	1.918(4)		

Statistics.

Table S11. General crystallographic data and statistics for hdcCOT at 100 K.

Crystallographic statistic	Data
Identification code	(4Z,9Z)-1,2,3,6,7,8-hexahydrodicyclopenta[a,e][8]annulene
CCDC number	2359798
Empirical formula	$C_{14}H_{16}$
Formula weight $(g mol^{-1})$	184.27
Temperature (Kelvin)	100
Crystal system	monoclinic
Space group	$P2_1/c$
a (Å)	6.6889(8)
b (Å)	21.463(3)
c (Å)	7.996(1)
$\alpha(°)$	90
$\beta(°)$	113.643(5)
$\gamma(°)$	90
V $(Å^3)$	1051.6(2)
Z	4
$\rho_{calc}(g mL^{-1})$	1.164
μ (mm^{-1})	0.068
F(000)	400.0
Crystal size (mm^3)	$0.05 \times 0.05 \times 0.05$
Radiation (Å)	synchotron ($\lambda = 0.7288$)
2θ range for data collection (°)	6.026 to 54.394
Index ranges	$-8 \leq h \leq 8, -26 \leq k \leq 26, -9 \leq l \leq 9$
Reflections collected	15072
Independent reflections	2164 [$R_{int} = 0.0676$, $R_{sigma} = 0.0481$]
Data/restraints/parameters	2164/0/151
Goodness-of-fit on F^2	1.045
Final R indexes [$I \geq 2\sigma(I)$]	$R_1 = 0.0466$, $wR_2 = 0.0466$
Final R indexes [all data]	$R_1 = 0.0582$, $wR_2 = 0.1215$
Largest diff. peak/hole (e $Å^{-3}$)	0.23/−0.28

Table S12. General crystallographic data and statistics for Th(hdcCOT)$_2$ at 150 K.

Crystallographic statistic	Data
Identification code	Th(hdcCOT)$_2$
CCDC number	2359799
Empirical formula	$C_{28}H_{32}Th$
Formula weight $(g mol^{-1})$	600.57
Temperature (Kelvin)	100
Crystal system	monoclinic
Space group	$P2_1/c$
a (Å)	11.1136(2)
b (Å)	11.7312(1)

c (Å)	8.7376(1)
α (°)	90
β (°)	112.081(2)
γ (°)	90
V (Å^3)	1055.62(3)
Z	2
ρ_{calc} (gmL^{-1})	1.889
μ (mm^{-1})	22.837
F(000)	580.0
Crystal size (mm^3)	0.169 × 0.148 × 0.038
Radiation (Å)	Cu Kα (λ = 1.54184)
2θ range for data collection (°)	8.586 to 159.65
Index ranges	$-14 \leq h \leq 14, -12 \leq k \leq 14, -11 \leq l \leq 10$
Reflections collected	22863
Independent reflections	2293 [R$_{int}$ = 0.0513, R$_{sigma}$ = 0.0225]
Data/restraints/parameters	2293/0/133
Goodness-of-fit on F^2	1.221
Final R indexes [I ≥ 2σ(I)]	R$_1$ = 0.0241, wR$_2$ = 0.0688
Final R indexes [all data]	R$_1$ = 0.0256, wR$_2$ = 0.0703
Largest diff. peak/hole (e Å^{-3})	0.78/−1.83

Table S13. General crystallographic data and statistics for Th(hdcCOT)$_2$ at 293 K.

Crystallographic statistic	Data
Identification code	Th(hdcCOT)$_2$
CCDC number	2359800
Empirical formula	C$_{28}$H$_{32}$Th
Formula weight (gmol^{-1})	600.57
Temperature (Kelvin)	100
Crystal system	monoclinic
Space group	$P2_1/c$
a (Å)	11.1354(8)
b (Å)	11.8050(6)
c (Å)	8.8126(6)
α (°)	90
β (°)	111.921(8)
γ (°)	90
V (Å^3)	1074.69(13)
Z	2
ρ_{calc} (gmL^{-1})	1.856
μ (mm^{-1})	6.949
F(000)	580.0
Crystal size (mm^3)	0.188 × 0.169 × 0.156
Radiation (Å)	Mo Kα (λ = 0.71073)
2θ range for data collection (°)	8.586 to 159.65
Index ranges	$-15 \leq h \leq 13, -15 \leq k \leq 16, -11 \leq l \leq 12$
Reflections collected	12589

Independent reflections	2818 [R_{int} = 0.0381, R_{sigma} = 0.0365]
Data/restraints/parameters	2818/0/133
Goodness-of-fit on F^2	1.059
Final R indexes [$I \geq 2\sigma(I)$]	R_1 = 0.0229, wR_2 = 0.0499
Final R indexes [all data]	R_1 = 0.0403, wR_2 = 0.0544
Largest diff. peak/hole (e Å^{-3})	0.51/-1.37

Table S14. General crystallographic data and statistics for U(hdcCOT)$_2$ at 100 K.

Crystallographic statistic	Data
Identification code	U(hdcCOT)$_2$
CCDC number	2359806
Empirical formula	$C_{28}H_{32}U$
Formula weight (gmol^{-1})	662.703
Temperature (Kelvin)	100.15
Crystal system	monoclinic
Space group	$P2_1/c$
a (Å)	11.1130(3)
b (Å)	11.6482(3)
c (Å)	8.5997(2)
$\alpha(°)$	90
$\beta(°)$	112.149(3)
$\gamma(°)$	90
V (Å^3)	1031.05(5)
Z	2
ρ_{calc}(gmL^{-1})	2.135
μ(mm^{-1})	7.897
F(000)	629.1
Crystal size (mm^3)	0.05 × 0.05 × 0.07
Radiation (Å)	Mo Kα (λ = 0.71073)
2θ range for data collection (°)	3.96 to 66.42
Index ranges	$-16 \leq h \leq 15, -16 \leq k \leq 17, -12 \leq l \leq 12$
Reflections collected	24133
Independent reflections	3568 [R_{int} = 0.0528, R_{sigma} = 0.0368]
Data/restraints/parameters	3568/0/133
Goodness-of-fit on F^2	0.976
Final R indexes [$I \geq 2\sigma(I)$]	R_1 = 0.0224, wR_2 = 0.0477
Final R indexes [all data]	R_1 = 0.0397, wR_2 = 0.0535
Largest diff. peak/hole (e Å^{-3})	1.39/-0.81

Table S15. General crystallographic data and statistics for U(hdcCOT)$_2$ at 295 K.

Crystallographic statistic	Data
Identification code	U(hdcCOT)$_2$
CCDC number	2359807

Empirical formula	$C_{28}H_{32}U$
Formula weight ($gmol^{-1}$)	606.56
Temperature (Kelvin)	100
Crystal system	monoclinic
Space group	$P2_1/c$
a (Å)	11.1517(3)
b (Å)	11.7253(2)
c (Å)	8.6987(2)
$\alpha(°)$	90
$\beta(°)$	112.081(3)
$\gamma(°)$	90
V ($Å^3$)	1053.99(5)
Z	2
$\rho_{calc}(gmL^{-1})$	1.911
$\mu(mm^{-1})$	7.712
F(000)	584.0
Crystal size (mm^3)	0.374 × 0.247 × 0.048
Radiation (Å)	Mo Kα (λ = 0.71073)
2θ range for data collection (°)	5.254 to 61.958
Index ranges	$-15 \le h \le 15, -16 \le k \le 15, -11 \le l \le 12$
Reflections collected	46124
Independent reflections	3123 [R_{int} = 0.0719, R_{sigma} = 0.0294]
Data/restraints/parameters	3123/0/133
Goodness-of-fit on F^2	1.049
Final R indexes [$I \ge 2\sigma(I)$]	R_1 = 0.0210, wR_2 = 0.0486
Final R indexes [all data]	R_1 = 0.036, wR_2 = 0.0533
Largest diff. peak/hole (e $Å^{-3}$)	0.75/−1.08

Table S16. General crystallographic data and statistics for Np(hdcCOT)$_2$ at 293 K.

Crystallographic statistic	Data
Identification code	Np(hdcCOT)$_2$
CCDC number	2359808
Empirical formula	$C_{28}H_{32}Np$
Formula weight ($gmol^{-1}$)	605.53
Temperature (Kelvin)	293(2)
Crystal system	monoclinic
Space group	$P2_1/c$
a (Å)	11.1581(3)
b (Å)	11.7251(2)
c (Å)	8.6952(2)
$\alpha(°)$	90
$\beta(°)$	112.142(3)
$\gamma(°)$	90
V ($Å^3$)	1053.70(5)
Z	2
$\rho_{calc}(gmL^{-1})$	1.909

$\mu(\text{mm}^{-1})$	4.943
F(000)	586.0
Crystal size (mm^3)	$0.2 \times 0.16 \times 0.1$
Radiation (Å)	Mo Kα ($\lambda = 0.71073$)
2θ range for data collection (°)	3.94 to 62.108
Index ranges	$-15 \leq h \leq 16, -16 \leq k \leq 16, -12 \leq l \leq 11$
Reflections collected	46074
Independent reflections	3108 [$R_{int} = 0.0443$, $R_{sigma} = 0.0204$]
Data/restraints/parameters	3108/0/133
Goodness-of-fit on F^2	1.067
Final R indexes [I $\geq 2\sigma$(I)]	$R_1 = 0.0184$, w$R_2 = 0.0397$
Final R indexes [all data]	$R_1 = 0.0314$, w$R_2 = 0.0436$
Largest diff. peak/hole (e Å^{-3})	1.01/-0.68

Table S17. General crystallographic data and statistics for Pu(hdcCOT)$_2$ at 100 K.

Crystallographic statistic	Data
Identification code	Pu(hdcCOT)$_2$
CCDC number	2359809
Empirical formula	$C_{28}H_{32}Pu$
Formula weight (gmol^{-1})	610.54
Temperature (Kelvin)	100
Crystal system	monoclinic
Space group	$P2_1/c$
a (Å)	11.10(2)
b (Å)	11.63(2)
c (Å)	8.583(2)
α(°)	90
β(°)	112.278(9)
γ(°)	90
V (Å^3)	1025(3)
Z	2
ρ_{calc}(gmL^{-1})	1.978
μ(mm^{-1})	3.672
F(000)	588.0
Crystal size (mm^3)	$0.25 \times 0.25 \times 0.08$
Radiation (Å)	synchotron ($\lambda = 0.7288$)
2θ range for data collection (°)	5.426 to 52.082
Index ranges	$-13 \leq h \leq 13, -14 \leq k \leq 14, -10 \leq l \leq 10$
Reflections collected	12668
Independent reflections	1877 [$R_{int} = 0.0832$, $R_{sigma} = 0.0576$]
Data/restraints/parameters	1877/0/133
Goodness-of-fit on F^2	1.108
Final R indexes [I $\geq 2\sigma$(I)]	$R_1 = 0.0403$, w$R_2 = 0.1157$
Final R indexes [all data]	$R_1 = 0.0495$, w$R_2 = 0.1268$
Largest diff. peak/hole (e Å^{-3})	1.41/-1.80

Table S18. General crystallographic data and statistics for Pu(hdcCOT)$_2$ at 296 K.

Crystallographic statistic	Data
Identification code	Pu(hdcCOT)$_2$
CCDC number	2359810
Empirical formula	C$_{28}$H$_{32}$Pu
Formula weight (gmol^{-1})	610.53
Temperature (Kelvin)	296.15
Crystal system	monoclinic
Space group	$P2_1/c$
a (Å)	11.187(4)
b (Å)	11.727(3)
c (Å)	8.691(3)
α(°)	90
β(°)	112.24(4)
γ(°)	90
V (Å^3)	1055.3(6)
Z	2
ρ_{calc}(gmL^{-1})	1.921
μ(mm^{-1})	3.135
F(000)	588.0
Crystal size (mm^3)	0.363 × 0.3 × 0.171
Radiation (Å)	Mo Kα (λ = 0.71073)
2θ range for data collection (°)	3.934 to 64.476
Index ranges	$-16 \le h \le 16, -17 \le k \le 17, -12 \le l \le 12$
Reflections collected	106857
Independent reflections	3515 [R$_{int}$ = 0.0996, R$_{sigma}$ = 0.0220]
Data/restraints/parameters	3515/16/133
Goodness-of-fit on F^2	1.176
Final R indexes [I $\ge$ 2σ(I)]	R$_1$ = 0.0433, wR$_2$ = 0.1174
Final R indexes [all data]	R$_1$ = 0.0524, wR$_2$ = 0.1234
Largest diff. peak/hole (e Å^{-3})	2.49/−2.24

Table S19. Comparison of geometric data for the M(hdcCOT)$_2$ and M(COT)$_2$ complexes. Data for M(COT)$_2$ (M = Th, U, Np, and Pu) are from literature.[31–32] Highlighted rows represent data collected at cryogenic temperatures (T ≤ 150K)

Molecule	a	b	c	β	V (Å^3)
Th(COT)$_2$	7.058(1)	8.819(2)	10.704(2)	98.44(3)	659.0(9)
U(COT)$_2$	7.084(3)	8.710(3)	10.631(5)	98.75(3)	648(1)
Np(COT)$_2$	7.124(4)	8.687(3)	10.606(1)	98.85(4)	648.6 (4)
Pu(COT)$_2$	7.0689(3)	8.6881(3)	10.5306(4)	98.989(4)	638.80(4)
Th(hdcCOT)$_2$	11.1136(2)	11.7312(1)	8.7376(1)	112.081(2)	1055.6(3)
	11.1354(8)	11.8050(6)	8.8126(6)	111.921(8)	1074.7(1)
U(hdcCOT)$_2$	11.1130(3)	11.6482(3)	8.5997(2)	112.149(3)	1031.05(5)
	11.1517(3)	11.7253(2)	8.6987(2)	112.081(3)	1053.99(5)
Np(hdcCOT)$_2$	11.1581(3)	11.7251(2)	8.6952(2	112.142(3)	1053.70(5)
Pu(hdcCOT)$_2$	11.10(2)	11.63(2)	8.583(2)	112.278(9)	1025(3)
	11.187(4)	11.727(3)	8.691(3)	112.24(4)	1055.3(6)

Table S20. Comparison of interatomic distance data for the M(hdcCOT)$_2$ and M(COT)$_2$ complexes. Data for M(COT)$_2$ (M = Th, U, Np, and Pu) are from literature.[31–32] Unless otherwise noted, the data cited in this table was collected at approximately 293 K.

Molecule	Ionic Radius (Å)	⟨M−C$_C$⟩ (Å)	⟨M−C$_H$⟩ (Å)	⟨M−C⟩ (Å)	⟨M···Z⟩^{b} (Å)
Th(COT)$_2$	1.14	---------------------	---------------------	2.701(4)	2.0036(5
Th(hdcCOT)$_2$		2.748(4)	2.706(5)	2.73(2)	2.006(1)
U(COT)$_2$	1.09	---------------------	---------------------	2.647(4)	1.9264(5)
U(hdcCOT)$_2$		2.701(4)	2.647(3)	2.67(3)	1.932(1)
Np(COT)$_2$	1.08	---------------------	---------------------	2.630(3)	1.9088(3)
Np(hdcCOT)$_2$		2.690(2)	2.640(4)	2.66(3)	1.9286(9)
Pu(COT)$_2$^{a}	1.06	---------------------	---------------------	2.640(4)	1.885(2)
Pu(hdcCOT)$_2$		2.682(7)	2.63(1)	2.65(3)	1.918(4)

^{a} Data collected at 150 K.

6. Computational details

Geometry optimization. Restrained (only hydrogen positions were optimized) and full geometry optimizations were carried out employing Kohn-Sham DFT calculations in the 2023 release of the Amsterdam Density Functional (ADF) suite. The PBE0 hybrid functional[33] with 25% exact exchange was used in conjunction with an all-electron Slater type orbital (STO) triple-zeta doubly-polarized (TZ2P) quality basis set for Th and a double-zeta polarized (DZP) STO basis set for non-metal atoms (C, H).[34] The functional was chosen based on its typically good performance for molecular properties.[33–35] Relativistic effects were incorporated via the scalar relativistic zeroth-order regular approximation (ZORA) Hamiltonian.[36] The geometry optimizations were carried out both in the gas phase as well as using the conductor-like screening model (COSMO)[37] with parameters for tetrahydrofuran (THF). The average Th–C distance in Th(COT)$_2$ is optimized to be 2.718 Å and 2.717 Å in the gas and solution phase, respectively, while the optimized Th−C distances for Th(hdcCOT)$_2$ are 2.708 Å (1)/2.776 Å (2) and 2.706 Å (1)/2.778 Å (2) respectively (numbers 1 and 2 in parentheses correspond to the two different C-centers in the 8-membered ring of hdcCOT). These bond parameters from the fully optimized structures (both in the gas and solution phase) are in good agreement with the X-ray crystallographic geometries, indicating that the crystal structures closely resemble the structures of the complexes as they would be expected to appear in solution or gas phase. Further analyses and calculations were performed with the fully-optimized crystal structures in THF solvent. Fragment orbitals (FOs) for the metal in its +4 ionic state and the ligands in

their −2 charge states were generated in the form of symmetrized fragment orbitals (SFOs) [38–39] as available in the ADF program. The fragment-based calculations used COSMO to model the presence of the THF. Natural charges on the metal and ligand were calculated using natural population analysis (NPA) as generated by the NBO program (version 6.0) interfaced with ADF.

Calculated spectra. TDDFT calculations of the absorption spectra of the Th complexes were performed using Gaussian 16 (G16) revision C.01 [40] with the PBE0 functional along with ECP60MWB pseudopotentials [40–42] and matching segmented valence basis sets for the metal center. The Gaussian-type def2-SVP basis set [43–44] was used for the other atoms. Solvent effects were incorporated by using the polarizable continuum model (PCM) [45] for THF. A total of 80 excited states were generated for $Th(COT)_2$ and $Th(hdcCOT)_2$ complexes respectively. Note, however, that 32 and 39 excited states, respectively, were sufficient to cover excitations in the range up to 4.0 eV. For the calculated TDDFT spectra a Gaussian broadening with $\sigma = 0.2$ eV was used. The most intense transitions were analyzed via natural transition orbitals (NTOs). [46] Orbital visualizations are in the form of ±0.04 isosurfaces.
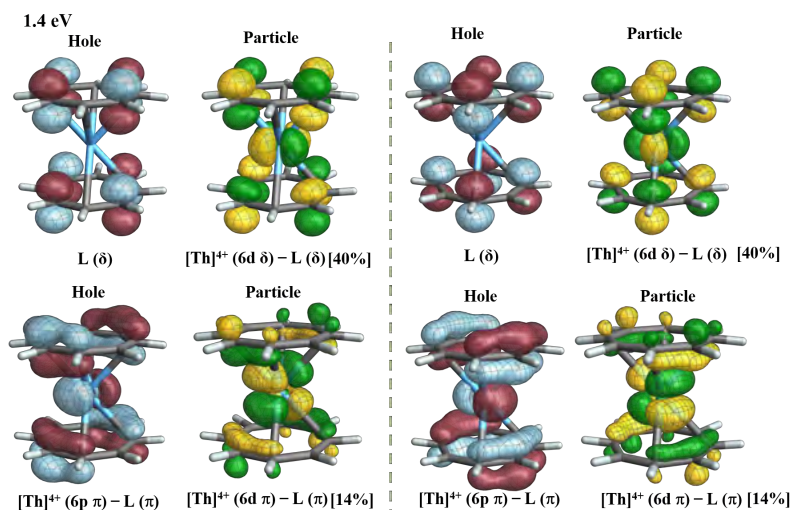
1.4 eV

Fig. S32. NTOs corresponding to the electronic transition calculated at 1.4 eV for Th(COT)$_2$ complex (in THF). Antibonding metal-ligand orbital combinations are indicated by a minus sign which does not necessarily mean equal magnitudes of the coefficients.
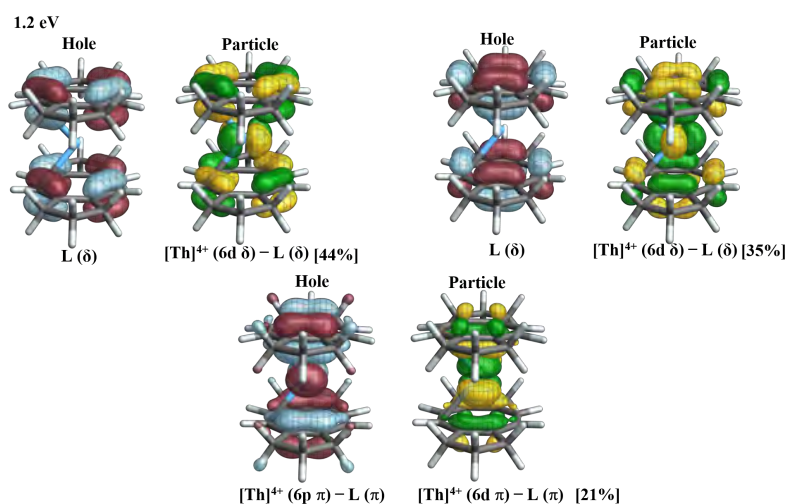
1.2 eV

Fig. S33. NTOs corresponding to the transition at 1.2 eV in the UV-Vis spectrum of Th(hdcCOT)$_2$ complex (in THF). Antibonding metal-ligand orbital combinations are indicated by a minus sign which does not necessarily mean equal magnitudes of the coefficients.

3.4 eV

Hole	Particle	Hole	Particle

[Th]$^{4+}$ (6p π) − L (π) [Th]$^{4+}$ (6d π) − L (π) [40%] [Th]$^{4+}$ (6p π) − L (π) [Th]$^{4+}$ (6d π) − L (π) [40%]

Hole	Particle	Hole	Particle

L (δ) [Th]$^{4+}$ (6d δ) − L (δ) [20%] L (δ) [Th]$^{4+}$ (6d δ) − L (δ) [20%]

Fig. S34. NTOs corresponding to the transition at 3.4 eV in the UV-Vis spectrum of Th(COT)$_2$ complex (in THF). Antibonding metal-ligand orbital combinations are indicated by a minus sign which does not necessarily mean equal magnitudes of the coefficients.

3.0 eV

Hole	Particle	Hole	Particle

[Th]$^{4+}$ (6p π) − L (π) [Th]$^{4+}$ (6d π) − L (π) [40%] [Th]$^{4+}$ (6p π) − L (π) [Th]$^{4+}$ (6d π) − L (π) [30%]

Hole	Particle	Hole	Particle

L (δ) [Th]$^{4+}$ (6d δ) − L (δ) [15%] L (δ) [Th]$^{4+}$ (6d δ) − L (δ) [15%]

Fig. S35. NTOs corresponding to the transition at 3.0 eV in the UV-Vis spectrum of Th(hdcCOT)$_2$ complex (in THF). Antibonding metal-ligand orbital combinations are indicated by a minus sign which does not necessarily mean equal magnitudes of the coefficients.
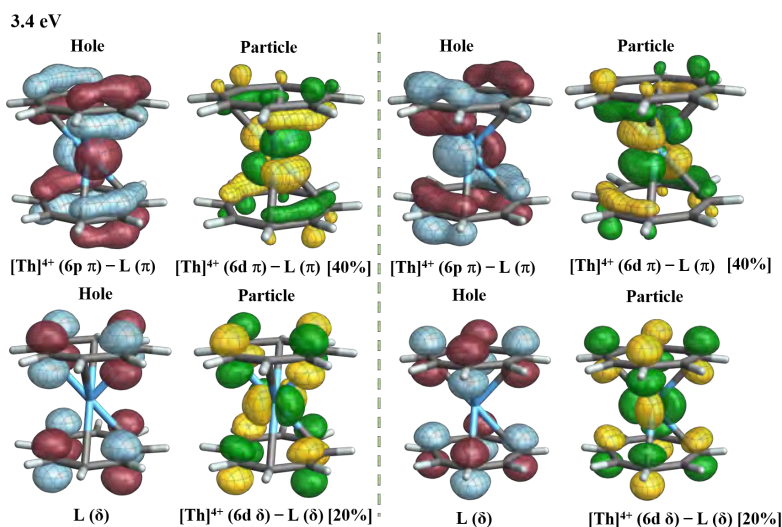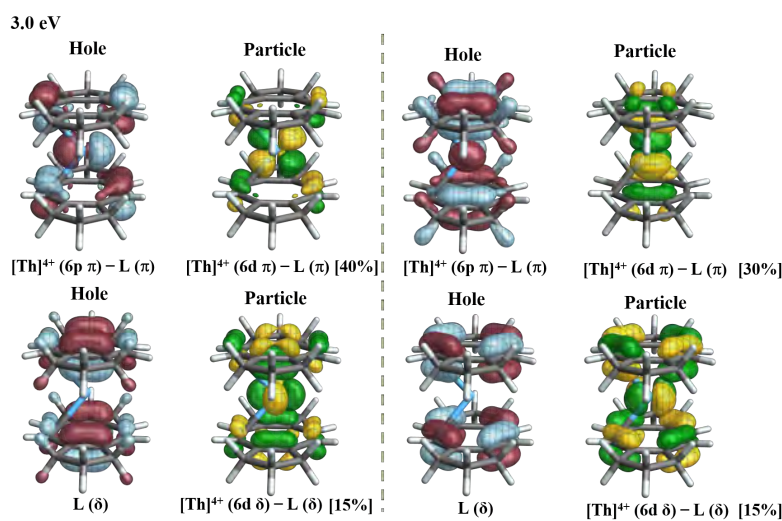
Table S21. Energies of the frontier orbitals of COT^{2-} and hdcCOT^{2-} in the gas phase and in THF.

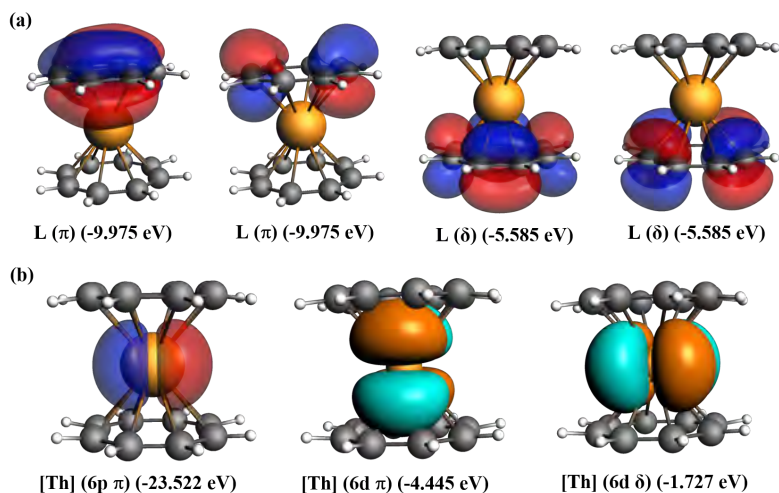| FO	COT^{2-}		hdcCOT^{2-}	
	gas	THF	gas	THF
HOMO	0.186	−0.093	0.163	−0.082
HOMO − 1	0.186	−0.093	0.160	−0.084
LUMO	0.330	0.087	0.286	0.088
LUMO + 1	0.362	0.126	0.288	0.097

Fig. S36. Ligand and Th fragment orbitals contributing to the NTOs of Th(COT)$_2$ complex.
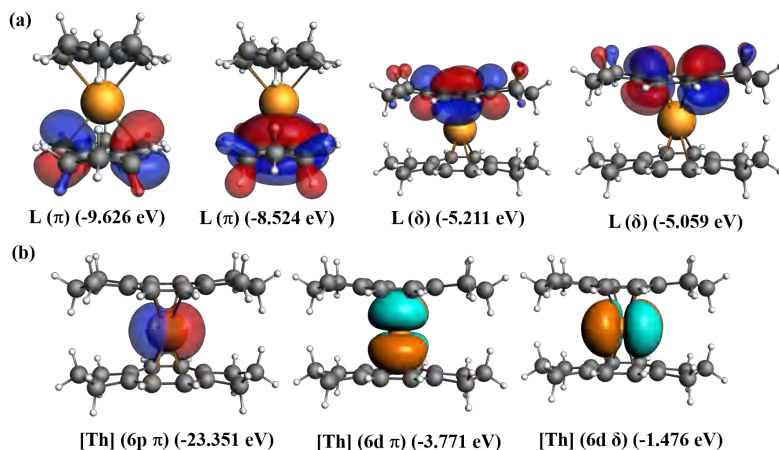
Fig. S37. Ligand and Th fragment orbitals contributing to the NTOs of Th(hdcCOT)$_2$ complex.

Table S22. Energies of the symmetrized fragment orbitals (SFOs) of Th(COT)$_2$, and Th(hdcCOT)$_2$ in the gas phase and in THF.

SFO site energies	Th(COT)$_2$	Th(hdcCOT)$_2$
SFO-1	−5.585	−5.059
SFO-2	−5.585	−5.211
π-SFO-1	−9.975	−8.524
π-SFO-2	−9.975	−9.626

Table S23. Natural Charges and electronic configuration on Th in Th(COT)$_2$ and Th(hdcCOT)$_2$ in THF.

	Th(COT)$_2$	Th(hdcCOT)$_2$
Natural Charge	1.006	1.166
Electronic Configuration	[Rn]$7s^{0.06}5f^{1.05}6d^{1.69}7p^{0.03}8s^{0.01}$	[Rn]$7s^{0.05}5f^{1.02}6d^{1.55}7p^{0.04}8s^{0.01}$

Thermal Destruction of Th(hdcCOT)$_2$
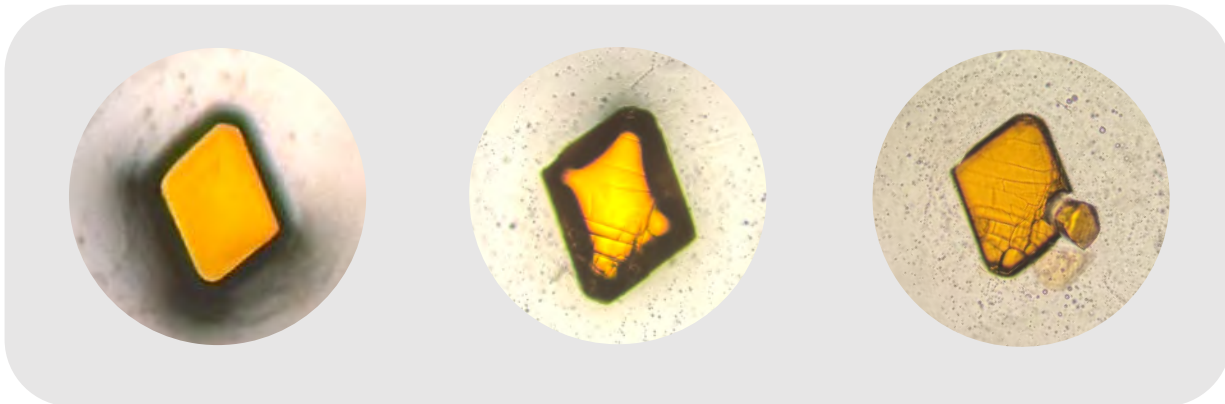
Fresh Crystal   **After 15 s at 100 K**   **After 60 s at 100 K**

Fig. S38. An example crystal of Th(hdcCOT)$_2$ cracking after being chilled for a set amount of time in a cryostream..

References

1. Yamamura, S.; Toda, M.; Hirata, Y. Modified Clemmensen Reduction: Cholestane *Org. Synth.* **1973,** *53,* 86.
2. Cantat, T.; Scott, B. L.; Kiplinger, J. L. Convenient access to the anhydrous thorium tetrachloride complexes $ThCl_4(DME)_2$, $ThCl_4(1,4\text{-dioxane})_2$ and $ThCl_4(THF)_{3.5}$ using commercially available and inexpensive starting materials *Chem. Commun.* **2010,** *46,* 919–921.
3. Travia, N. E.; Monreal, M. J.; Scott, B. L.; Kiplinger, J. L. Thorium-mediated ring-opening of tetrahydrofuran and the development of a new thorium starting material: preparation and chemistry of $ThI_4(DME)_2$ *Dalton Trans.* **2012,** *41,* 14514.
4. Hermann, J. A.; Suttle, J. F.; Hoekstra, H. R. Uranium(IV) Chloride. In *Inorganic Syntheses*; Inorganic Syntheses John Wiley & Sons, Inc.: Hoboken, NJ, USA, 2007.
5. Monreal, M. J.; Thomson, R. K.; Cantat, T.; Travia, N. E.; Scott, B. L.; Kiplinger, J. L. $UI_4(1,4\text{-dioxane})_2$, $[UCl_4(1,4\text{-dioxane})]_2$, and $UI_3(1,4\text{-dioxane})_{1.5}$: Stable and versatile starting materials for low- and high-Valent uranium chemistry *Organometallics* **2011,** *30,* 2031–2038.
6. Reilly, S. D.; Brown, J. L.; Scott, B. L.; Gaunt, A. J. Synthesis and characterization of $NpCl_4(DME)_2$ and $PuCl_4(DME)_2$ neutral transuranic An(IV) starting materials *Dalton Trans.* **2014,** *43,* 1498–1501.
7. Peterson, A.; Kelly, S. N.; Arino, T.; Gunther, S. O.; Ouellette, E. T.; Wacker, J. N.; Woods, J. J.; Teat, S. J.; Lukens, W. W.; Arnold, J.; Abergel, R. J.; Minasian, S. G. Formation of fully stoichiometric, oxidation-state pure neptunium and plutonium dioxides from molecular precursors *Inorg. Chem.* **2024,** *63,* 18417–18428.
8. Basunia, M. Nuclear Data Sheets for A = 237 *Nucl. Data Sheets* **2006,** *107,* 2323–2422.
9. Singh, B.; Tuli, J. K.; Browne, E. Nuclear Data Sheets for A = 233 *Nucl. Data Sheets* **2020,** *170,* 499–705.
10. Martin, M.; Nesaraja, C. Nuclear Data Sheets for A = 242 *Nucl. Data Sheets* **2022,** *186,* 263–395.
11. Chukreev, F. E.; Singh, B. Nuclear data sheets for A = 240 *Nucl. Data Sheets* **2004,** *103,* 325–388.
12. Shurshikov, E. N. Nuclear data sheets for A = 238 *Nucl. Data Sheets* **1988,** *53,* 601–676.
13. Ellis-Akovali, Y. A. Nuclear data sheets for A = 241 *Nucl. Data Sheets* **1985,** *44,* 407–461.
14. Fulmer, G. R.; Miller, A. J. M.; Sherden, N. H.; Gottlieb, H. E.; Nudelman, A.; Stoltz, B. M.; Bercaw, J. E.; Goldberg, K. I. NMR Chemical Shifts of Trace Impurities: Common Laboratory Solvents, Organics, and Gases in Deuterated Solvents Relevant to the Organometallic Chemist *Organometallics* **2010,** *29,* 2176–2179.
15. Bruker, A. S.; Bruker, A. Inc., Madison, Wisconsin, USA, 2004,(b) Sheldrick *Acta Cryst. A* **1990,** *46,* 467–473.
16. Sheldrick, G. SHELXT - Integrated space-group and crystal-structure determination *Acta Crystallogr. Sect. A* **2015,** *71,* 3–8.
17. Dolomanov, O. V.; Bourhis, L. J.; Gildea, R. J.; Howard, J. A. K.; Puschmann, H. OLEX2: a complete structure solution, refinement and analysis program *J. Appl. Crystallogr.* **2009,** *42,* 339–341.
18. Sheldrick, G. Crystal structure refinement with SHELXL *Acta Crystallogr. Sect. C* **2015,** *71,* 3–8.
19. "Crystalmaker is a a crystal and molecular structures program for Mac and Windows. (www.crystalmaker.com)", .
20. Ward, L. G. L.; Pipal, J. R. Anhydrous Nickel(II) Halides and their Tetrakis(ethanol) and 1,2-Dimethoxyethane Complexes. In *Inorganic Syntheses*; Inorganic Syntheses John Wiley & Sons, Inc.: Hoboken, NJ, USA, 1972.
21. Crochet, A.; Fromm, K. M. Polyether adducts of d-block metal compounds as starting materials for new cluster compounds *Z. Anorg. Allg. Chem.* **2010,** *636,* 1484–1496.
22. Wender, P. A.; Christy, J. P. Nickel(0)-Catalyzed [2 + 2 + 2 + 2] Cycloadditions of Terminal Diynes for the Synthesis of Substituted Cyclooctatetraenes *J. Am. Chem. Soc.* **2007,** *129,* 13402–13403.
23. Hiller, M.; Maier, M.; Wadepohl, H.; Enders, M. Paramagnetic NMR Analysis of Substituted Biscyclooctatetraene Lanthanide Complexes *Organometallics* **2016,** *35,* 1916–1922.
24. Orlova, A. P.; Bernbeck, M. G.; Rinehart, J. D. Designing Quantum Spaces of Higher Dimensionality from a Tetranuclear Erbium-Based Single-Molecule Magnet *J. Am. Chem. Soc.* **2024,** *146,* 23417–23425.
25. Goodwin, C. A. P.; Janicke, M. T.; Scott, B. L.; Gaunt, A. J. $[AnI_3(THF)_4]$ (An = Np, Pu) Preparation Bypassing An0 Metal Precursors: Access to Np^{3+}/Pu^{3+} Nonaqueous and Organometallic Complexes *J. Am. Chem. Soc.*

2021, *143,* 20680–20696.

26. Streitwieser, A. J.;   Dempf, D.;   La Mar, G. N.;   Karraker, D. G.;   Edelstein, N. Bis(1,3,5,7-tetramethylcyclooctatetraene)uranium(IV) and bis(1,3,5,7-tetramethylcyclooctatetraene)-neptunium(IV). Proton magnetic resonance spectrum and the question of f-orbital covalency *J. Am. Chem. Soc.* **1971,** *93,* 7343–7344.

27. Zalkin, A.; Templeton, D. H.; Luke, W. D.; Streitwieser, A. J. Synthesis and structure of dicyclopentenouranocene, U[C$_8$H$_6$(CH$_2$)$_3$]$_2$ *Organometallics* **1982,** *1,* 618–622.

28. Inc., T. M. "MATLAB version: 24.2 (R2024a)", 2022.

29. Luke, W. D. *The Synthesis and Characterization of Annulated Uranocenes. The Variable Temperature Proton NMR of Uranocenes,* PhD Thesis, U.C. Berkeley, 1980.

30. Karraker, D. G.; Stone, J. A.; Jones, E. R. J.; Edelstein, N. Bis(cyclooctatetraenyl)neptunium(IV) and bis(cyclooctatetraenyl)plutonium(IV) *J. Am. Chem. Soc.* **1970,** *92,* 4841–4845.

31. De Ridder, D. J. A.;   Rebizant, J.;   Apostolidis, C.;   Kanellakopulos, B.;   Dornberger, E. Bis(cyclooctatetraenyl)neptunium(IV) *Acta Crystallogr. Sect. C* **1996,** *52,* 597–600.

32. Windorff, C. J.; Sperling, J. M.; Albrecht-Schönzart, T. E.; Bai, Z.; Evans, W. J.; Gaiser, A. N.; Gaunt, A. J.; Goodwin, C. A. P.; Hobart, D. E.; Huffman, Z. K.; Huh, D. N.; Klamm, B. E.; Poe, T. N.; Warzecha, E. A Single Small-Scale Plutonium Redox Reaction System Yields Three Crystallographically-Characterizable Organoplutonium Complexes *Inorg. Chem.* **2020,** *59,* 13301–13314.

33. Adamo, C.; Barone, V. Toward reliable density functional methods without adjustable parameters: The PBE0 model *J. Chem. Phys.* **1999,** *110,* 6158–6170.

34. Van Lenthe, E.; Baerends, E. J. Optimized Slater-type basis sets for the elements 1–118 *J. Comput. Chem.* **2003,** *24,* 1142–1156.

35. Adamo, C.; Barone, V. Toward chemical accuracy in the computation of NMR shieldings: the PBE0 model *Chem. Phys. Lett.* **1998,** *298,* 113-119.

36. van Lenthe, E.; Baerends, E. J.; Snijders, J. G. Relativistic regular two-component Hamiltonians *J. Chem. Phys.* **1993,** *99,* 4597–4610.

37. Pye, C. C.; Ziegler, T. An implementation of the conductor-like screening model of solvation within the Amsterdam density functional package *Theor. Chem. Acc.* **1999,** *101,* 396–408.

38. te Velde, G.; Bickelhaupt, F. M.; Baerends, E. J.; Fonseca Guerra, C.; van Gisbergen, S. J. A.; Snijders, J. G.; Ziegler, T. Chemistry with ADF *J. Comput. Chem.* **2001,** *22,* 931–967.

39. Dognon, J.-P.; Clavaguéra, C.; Pyykkö, P. A predicted organometallic series following a 32-electron principle: An@C$_{28}$ (An = Th, Pa$^+$, U^{2+}, Pu^{4+}) *J. Am. Chem. Soc.* **2009,** *131,* 238–243.

40. Frisch, M. J. *et al.* "Gaussian~16 Revision C.01", 2016 Gaussian Inc. Wallingford CT.

41. Andrae, D.; Häuβermann, U.; Dolg, M.; Stoll, H.; Preuβ, Energy-adjusted *ab initio* pseudopotentials for the second and third row transition elements *Theoret. Chim. Acta* **1990,** *77,* 123–141.

42. Cao, X.; Dolg, M. Relativistic energy-consistent ab initio pseudopotentials as tools for quantum chemical investigations of actinide systems *Coord. Chem. Rev.* **2006,** *250,* 900–910.

43. Dunning, Jr, T. H. Gaussian basis sets for use in correlated molecular calculations. I. The atoms boron through neon and hydrogen *J. Chem. Phys.* **1989,** *90,* 1007–1023.

44. Schäfer, A.; Horn, H.; Ahlrichs, R. Fully optimized contracted Gaussian basis sets for atoms Li to Kr *J. Chem. Phys.* **1992,** *97,* 2571–2577.

45. Tomasi, J.; Persico, M. Molecular interactions in solution: An overview of methods based on continuous distributions of the solvent *Chem. Rev.* **1994,** *94,* 2027–2094.

46. Martin, R. L. Natural transition orbitals *J. Chem. Phys.* **2003,** *118,* 4775–4777.

Appdenix

Table S24. Tabulated ^{1}H NMR data of relevant impurities to this manuscript in pyridine-d$_5$.

	Proton	Multiplicity	Chemical shift (ppm)
solvent residual signals			7.19
			7.55
			8.71
Acetonitrile	CH$_3$	s	1.85
Chlorobenzene	CH(2,4,6)	m	7.22
	CH(3,5)	m	7.36
18-crown-6	CH$_2$	s	3.62
2.2.2. cryptand	CH$_2$	t, 12	2.63
	CH$_2$	t, 12	3.61
	CH$_2$	s, 12	3.70
Diethyl ether	CH$_3$	t, 6	1.10
	CH$_2$	q, 4	3.33
1,2-Dimethoxyethane	CH$_3$	s, 3	3.25
	CH$_2$	s, 4	3.47
Fluorobenzene	CH(2,4,6)	m	7.11
	CH(3,5)	m	7.29
H grease	CH$_3$	br, m	0.87
	CH$_2$	br, m	1.30
Hexamethyldisiloxane	CH$_3$	s	0.10
n-Hexane	CH$_3$	t	0.82
	CH$_2$	m	1.16
M grease	CH$_3$	br, m	0.84
	CH$_2$	br, m	1.31
n-Pentane	CH$_3$	t	0.79
	CH$_2$	m	1.16
Silicone grease	CH$_3$	s	0.32
Tetrahydrofuran	CH$_2$	m	1.59
	CH$_2$	m	3.63
Toluene	CH$_3$	s	2.20
	CH(2,4,6)	m	7.16
	CH(3,5)	m	7.26

Table S25. Tabulated ^{1}H NMR data of relevant impurities to this manuscript in pyridine-d$_5$.

	Proton	Multiplicity	Chemical shift (ppm)
		t	123.5
solvent residual signals		t	135.5
		t	149.5
Acetonitrile	CH$_3$		0.65
	CN		117.11
Chlorobenzene	CH(4)		126.64
	CH(2,6)		128.49

	CH(3,5)		129.96
	C(1)		133.91
18-crown-6	CH$_2$		70.51
2.2.2. cryptand	CH$_2$		56.36
	CH$_2$		69.91
	CH$_2$		70.74
Diethyl ether	CH$_3$		65.39
	CH$_2$		15.11
1,2-Dimethoxyethane	CH$_3$		58.20
	CH$_2$		71.65
Fluorobenzene	CH(4)	d, C−F J = 20.8 Hz	115.18
	CH(2,6)	d, C−F J = 3.1 Hz	124.2
	CH(3,5)	d, C−F J = 7.8 Hz	130.18
	C(1)	d, C−F J = 244.4 Hz	162.78
H grease	CH$_2$		29.61
Hexamethyldisiloxane	CH$_3$		2.00
n-Hexane	CH$_3$		13.84
	CH$_2$ (2,5)		22.46
	CH$_2$ (3,4)		31.34
M grease	CH$_2$		29.61
n-Pentane	CH$_3$		13.76
	CH$_2$		22.12
	CH$_2$		33.79
Silicone grease	CH$_3$		1.33
Tetrahydrofuran	CH$_2$		25.41
	CH$_2$		57.44
Toluene	CH$_3$		20.92
	CH(4)		125.37
	CH(3,5)		128.27
	CH(2,6)		129.02
	C(1)		137.64